Impacts of Enhanced Weathering on biomass production for negative emission technologies and soil hydrology

Wagner de Oliveira Garcia*[1], Thorben Amann[1], Jens Hartmann[1], Kristine Karstens[2], Alexander Popp[2], Lena R. Boysen[3], Pete Smith[4], Daniel Goll[5,6]

[1]Institute for Geology, Center for Earth System Research and Sustainability, Universität Hamburg, Germany
[2]Potsdam Institute for Climate Impact Research (PIK), Germany
[3]Max Planck Institute for Meteorology, Germany
[4]Institute of Biological and Environmental Sciences, School of Biological Sciences, University of Aberdeen
[5]Laboratoire des Sciences du Climat et de l'Environnement, CEA CNRS UVSQ, 91190 Gif-sur-Yvette, France
[6]Institute of Geography, University Augsburg, Germany

**Correspondense to*: Wagner de Oliveira Garcia (wagner.o.garcia@gmail.com) ORCID: https://orcid.org/0000-0001-9559-0629

Supplementary information

Summary

Abbreviation

Mg, Ca, K, P	Macronutrients, respectively: Magnesium, Calcium, Potassium, Phosphorus	
RCP4.5	Representative Concentration Pathway for radiative forcing value in 2100 of +4.5 W m^{-2} relative to pre-industrial values.	
AR	Afforestation/Reforestation	
BECCS	Bio-Energy with Carbon Capture and Storage	
PTF	Pedotransfer Functions	
Fine basalt powder	Basalt powder texture of 15.6% clay, 83.8% silt and 0.6% fine sand	
Coarse basalt powder	Basalt powder texture of 15.6% clay, 53.8% silt and 30.6% fine sand	
S	Sand texture	[wt %]
C	Clay texture	[wt %]
OM	Soil organic matter	[wt %]
θ_{1500} and θ_{33} [a]	Moisture for a pressure head of -1500 kPa and of -33 kPa.	[wt %]
$\theta_{(S-33)}$ [a]	0 kPa to -33 kPa moisture	[wt %]
θ_S [a]	Saturated (0 kPa) moisture	[wt %]

K_S[a]	Saturated soil hydraulic conductivity	[mm h^{-1}]
λ[a]	Slope of logarithmic tension-moisture curve	[-]
G_{cor}	Corrected soil texture after basalt application	[-]
G_{ini}	Initial soil texture	[-]
V_{cell}	Raster cell volume	[km^3]
ρ_{bulk_cell}	Soil bulk density	[$kg.km^{-3}$]
M_{soil_cell}	Total sediment mass	[kg]
OM_c	Corrected organic matter content	[wt %]
OM_{cell}	Organic matter mass	[kg]
M_{b_cell}	Basalt mass	[kg]
M_{soil_cell}	Soil mass	[kg]
G_{basalt}	Basalt texture	[-]
G_{bs}	Texture fractions of resulting mixture of basalt plus soil	[-]

[a] equation from (Saxton and Rawls, 2006).

S1. Introduction

The stoichiometric ratios used to estimate the median and ranges (5^{th} and 95^{th} percentiles) macronutrient demand by afforestation in the main text section "Nutrient demand Afforestation/Reforestation" are presented as an excel file "S2.xlsx". The different P supply maps (Fig. S1, Fig. S2, and Fig. S3) for the period of 2006 – 2099, which were used to estimate the geogenic P supply scenarios one (P from weathering plus atmospheric P deposition) and two (the same as scenario one plus inorganic labile P and organic P) that could potentially be available for plant nutrition are presented in this supplement within chapter S2. The used median and ranges (5^{th} and 95^{th} percentiles) for the macronutrients within rhyolite and dacite (acid rocks), andesite (intermediate rock) and basalt (basic rock), corresponding to different rock exemplars of each rock class are presented in chapter S3 (Fig. S4). The chemical composition is used to estimate the potential macronutrient supply by dissolution of each rock type. In the chapter S4, we present the results that were not presented in main text for EW coupled with AR that are: the area covered by forest and the C content for the 94 years (Kracher, 2017) for an N-unlimited and an N-limited scenario in Fig. S5; the potential macronutrient supply by the dissolution of the previous cited rocks for covering a range of P gaps of <<1 to 17.1 g P m^{-2} (Fig. S6); the potential P gaps for an N-unlimited AR scenario (Fig. S9 and Fig. S15) and for an N-limited AR scenario (Fig. S10 and Fig. S16). The related C-fixation reduction for an N-unlimited AR scenario (Fig. S13 and Fig. S19) and for an N-limited AR scenario (Fig. S14 and Fig. S20) for each P budget scenario for wood and foliar chemistry corresponding to 5^{th} and 95^{th} percentiles; the potential P gaps and C-fixation reduction mean values for the N-saturated AR scenario (Fig. S21 and Fig. S22); the necessary basalt powder deployment to bridge the estimated P gaps of each geogenic P supply scenario for mean and range (5^{th} and 95^{th} percentiles) of wood and foliar chemistry (respectively Fig. S7, Fig. S11, and Fig. S17) for an N-unlimited AR scenario and for an N-limited AR scenario (Fig. S8, Fig. S12, and Fig. S18). The soil hydrology impacts as a function of deployed rock mass for a coarse and a fine texture is presented in chapter S5 for the P budget scenario two (Fig. S23). The soil hydrology impacts by bridging the P gap of geogenic P supply from scenario one for a fine and a coarse textured basalt powder is presented (Fig. S24 and Fig. S25). For P budget of geogenic P supply scenario two, the impacts on soil hydraulic conductivity and plant available water could be neglected (Fig. S26 and Fig. S27). The results for impacts in soil hydrology are presented for the N-unlimited AR scenario, since the required amount of rock powder to bridge the projected P gaps will be higher than for an N-limited scenario. Consequently, the changes in soil hydraulic properties for the N-unlimited AR scenario will be more remarkable than for the N-limited AR-scenario. A detailed documentation on the calculation of the soil texture changes due rock powder application, and used pedotransfer equations are given.

S2. Geogenic nutrient pools

The atmospheric P deposition simulations from Wang et al. (2017) considered the recent 2006 – 2013 period while the years of 2030, 2050, and 2100 were for an RCP4.5 scenario. The grid cell size was of 1° and were regridded to 2°×2° spatial resolution fields by nearest neighbor interpolation. The time-gaps were closed by linear regression and the total atmospheric P deposition contribution was quantified by summing up the atmospheric deposition values from 2006 to 2099 (Fig. S1).

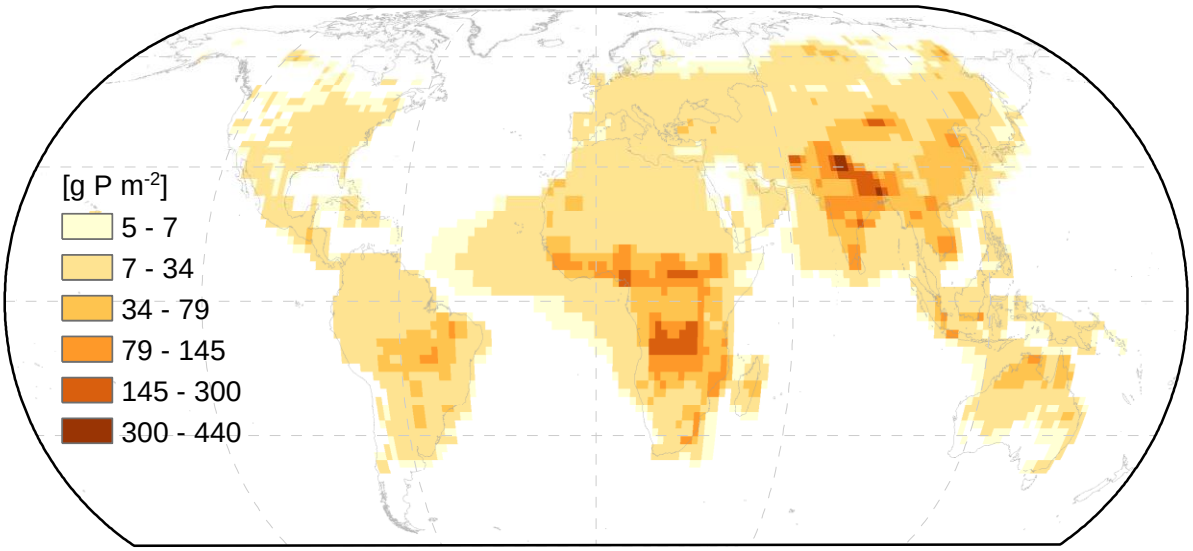

Fig. S1: Cumulative atmospheric P deposition for 2006 – 2099 according to Wang et al. (2017). Map generated with ESRI ArcGIS 10.6 (http://www.esri.com).

The total soil P map from Yang et al. (2014) was used as estimation of the projected long term available P in the soil system (Fig. S2). Similarly to the atmospheric P deposition rasters, it was resampled to 2°×2° spatial resolution fields by nearest neighbour interpolation.

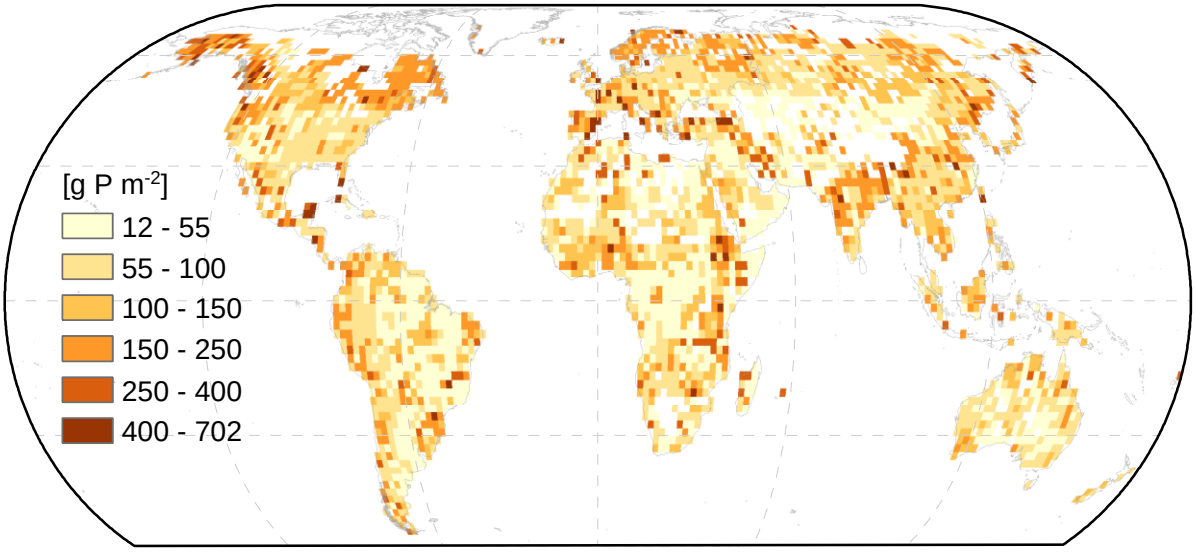

Fig. S2: Total inorganic labile P and organic P in the soil for a depth of 0.5 m according to Yang et al. (2014). Map generated with ESRI ArcGIS 10.6 (*http://www.esri.com*).

The related P release by weathering was obtained from Hartmann et al. (2014) and a relationship between air temperature and weathering rate was used, whereby P weathering increases by 9% per 1ºC increase (Goll et al., 2014) without accounting for P concentration changes in primary and secondary P minerals. The resulting raster was regridded to 2°×2° spatial resolution fields by nearest neighbour interpolation (Fig. S3).

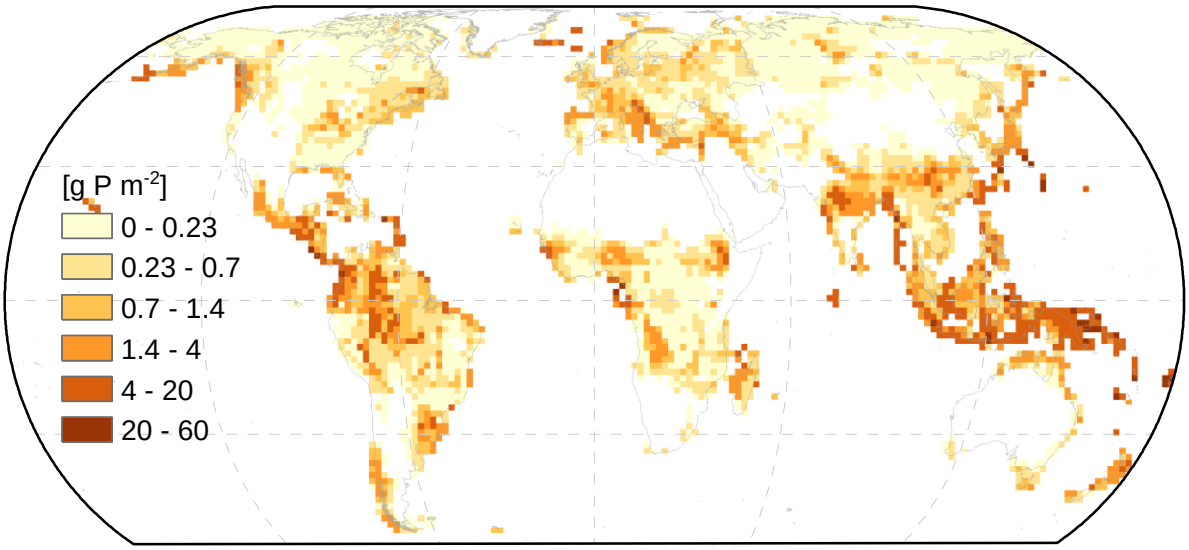

Fig. S3: Cumulative weathering P release for the 21st century (2006 – 2099) based on Hartmann et al. (2014) accounting for weathering rate changes related to temperature increase (Goll et al., 2014). Map generated with ESRI ArcGIS 10.6 (*http://www.esri.com*).

S3. EW as nutrient source

The median and ranges (5th and 95th percentiles) from rhyolite and dacite (acid rocks), andesite (intermediate rock) and basalt (basic rock) chemical composition (Fig. S4) were obtained from a rock chemistry database compilation (Earthchem web portal, http://www.earthchem.org, accessed on 2017-07-14).

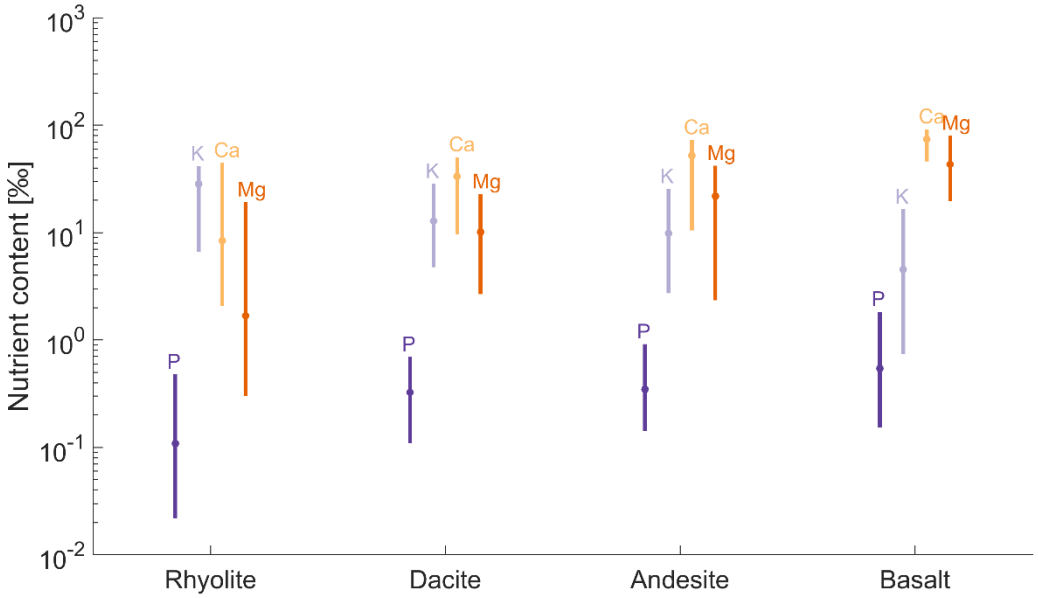

Fig. S4: Statistical data of major element concentration in rocks, median values (filled circles) and range (5th and 95th percentiles, whiskers). Values from a database downloaded from the Earthchem webportal (http://www.earthchem.org).

S4. EW coupled with AR

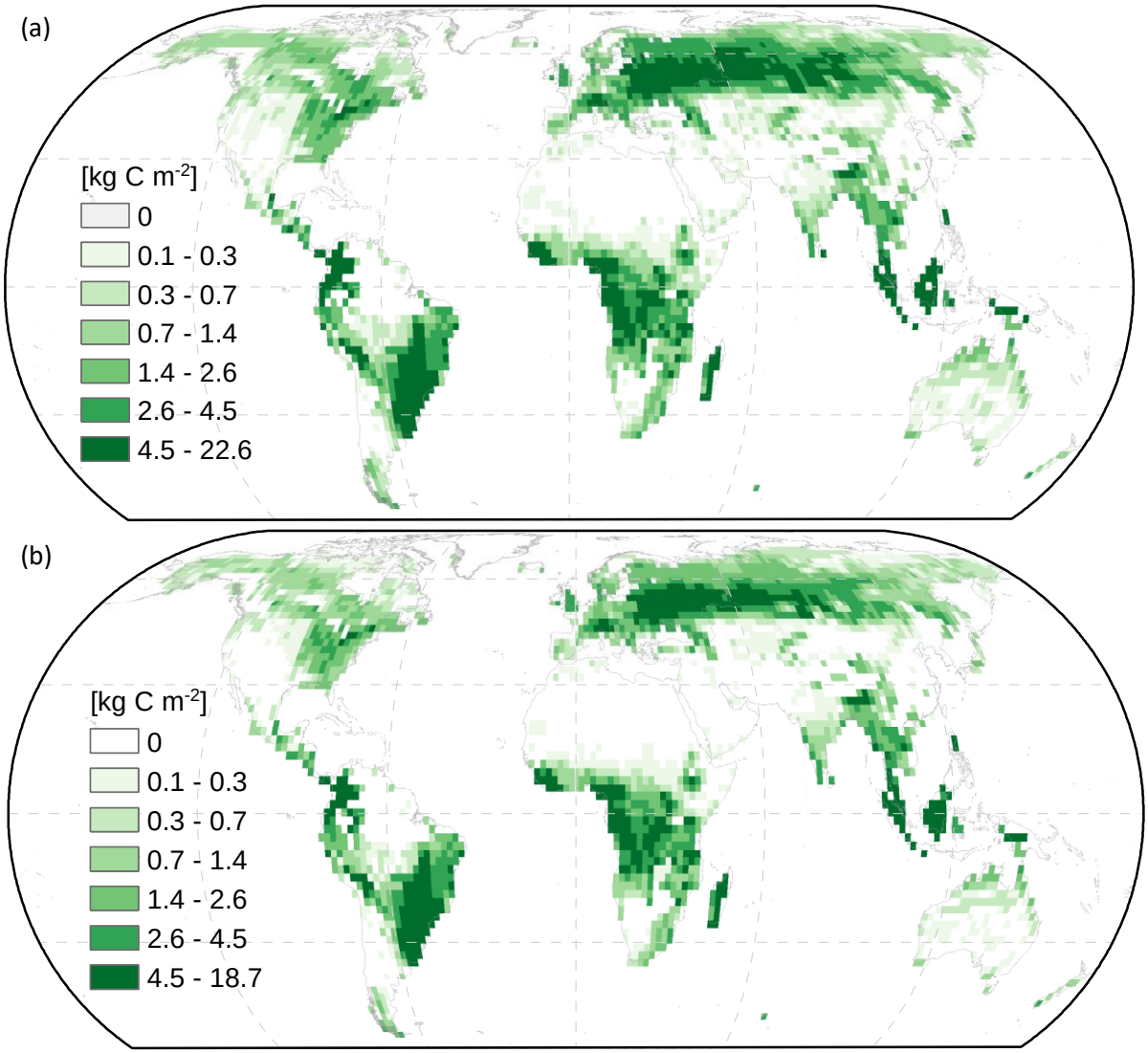

Fig. S5: AR carbon for the 21st century (2006 – 2099) period of forest growth for a RCP4.5 scenario, according to Kracher (2017). a) For an N-unlimited AR scenario. b) For an N-limited AR scenario. Map generated with ESRI ArcGIS ver. 10.6 (*http://www.esri.com*).

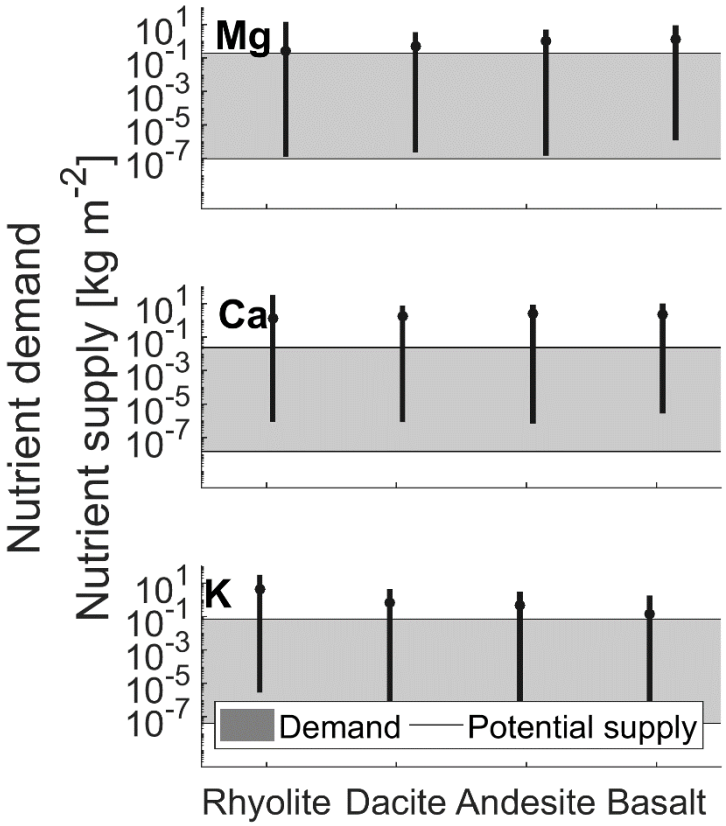

Fig. S6: Potential macronutrient (Mg, Ca, and K) supply of different rocks for closing projected P gaps of <<1 to 17.1 g P m^{-2}. Median and ranges (5^{th} and 95^{th} percentiles) of potential supply based on rock chemistry.

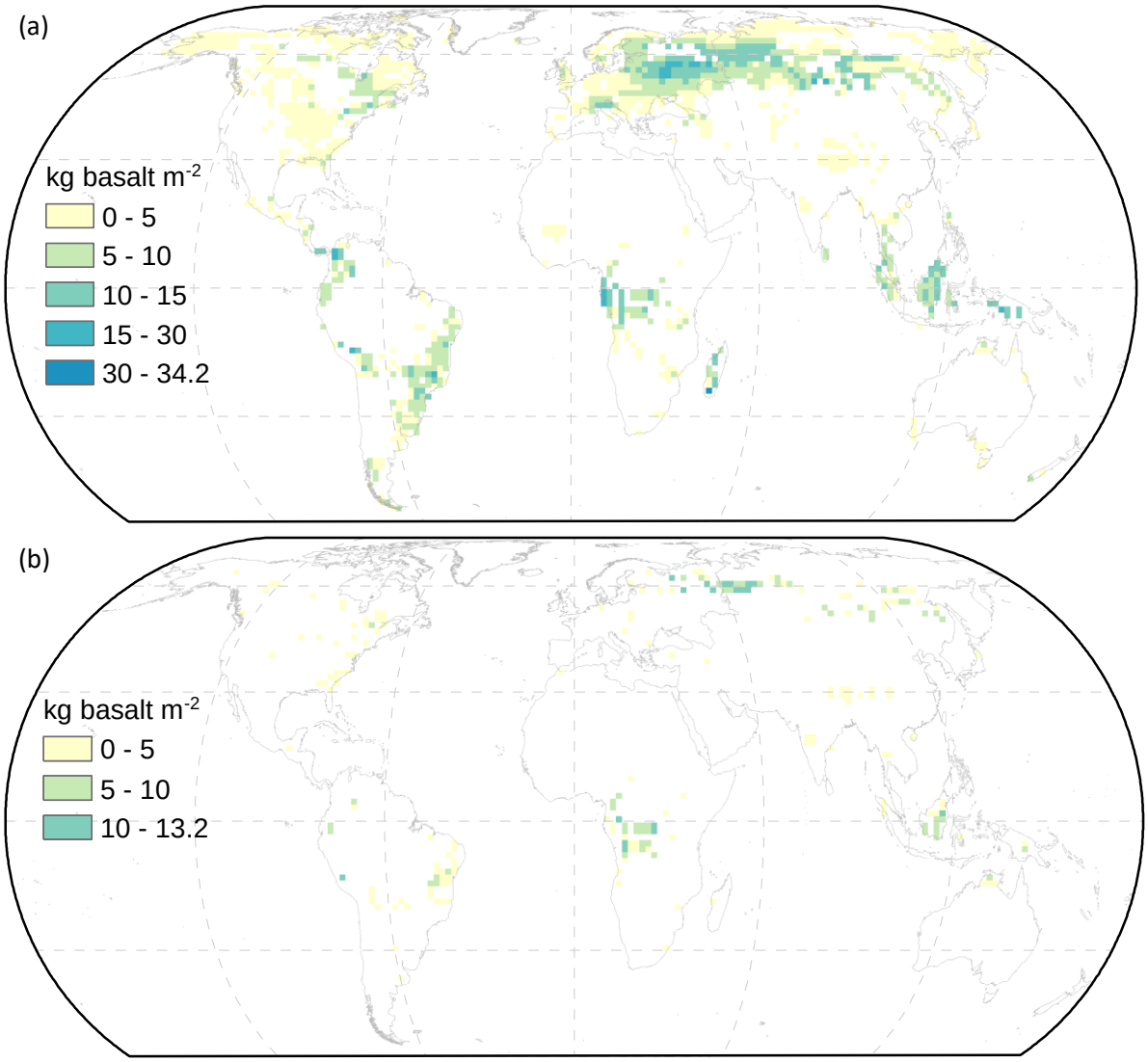

Fig. S7: Basalt deployment necessary to close P gaps from P budget scenarios of Fig. S22. a) Geogenic P supply scenario one (geogenic P from weathering plus atmospheric P deposition as source of P). b) Geogenic P supply scenario two (geogenic P from soil inorganic labile P and organic P pools plus atmospheric P deposition and P from weathering as source of P). Map generated with ESRI ArcGIS 10.6 (*http://www.esri.com*).

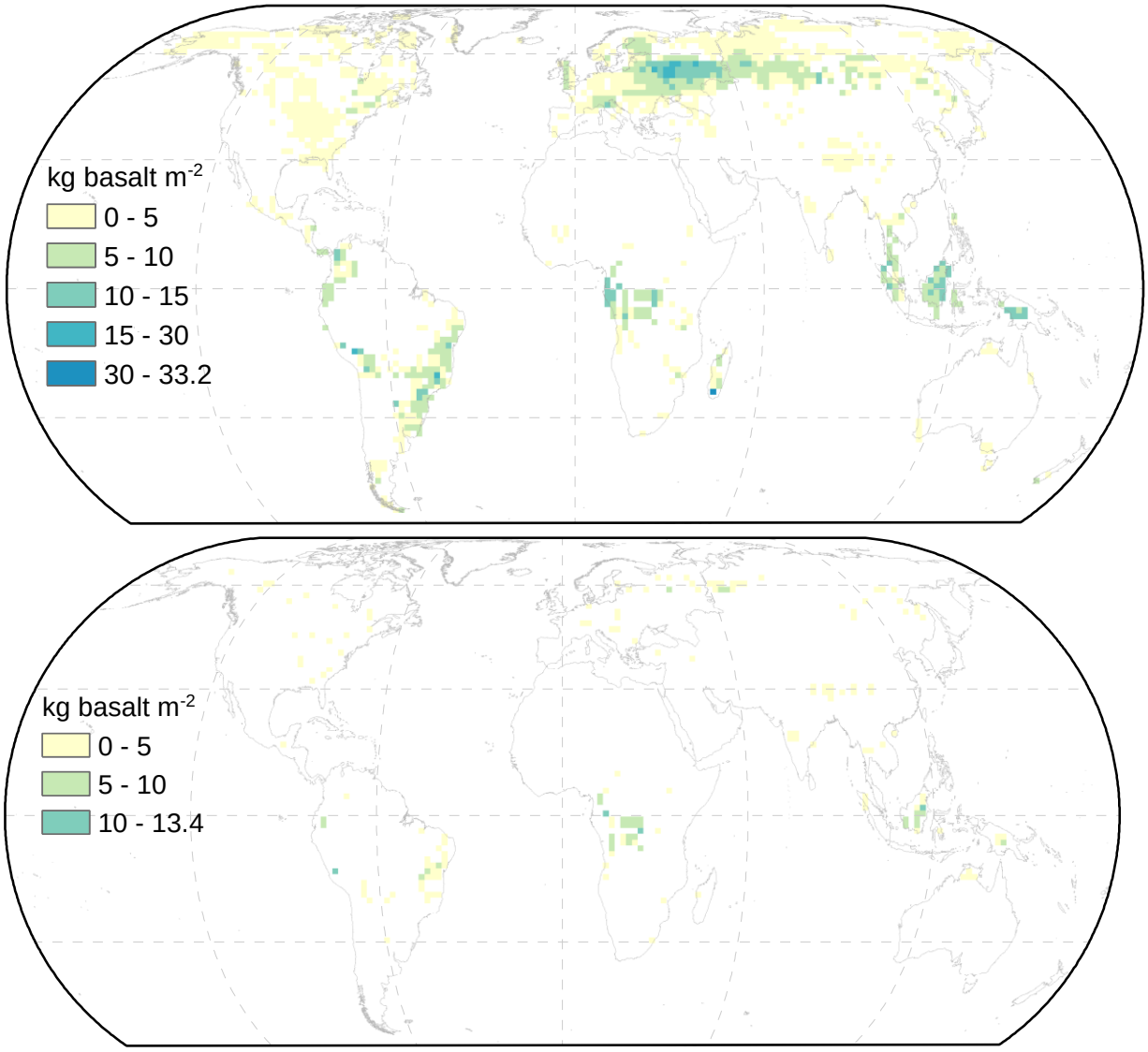

Fig. S8: Basalt deployment necessary to close P gaps from P budget scenarios of main text Fig. 2. a) Geogenic P supply scenario one (geogenic P from weathering plus atmospheric P deposition as source of P). b) Geogenic P supply scenario two (geogenic P from soil inorganic labile P and organic P pools plus atmospheric P deposition and P from weathering as source of P). Map generated with ESRI ArcGIS 10.6 (*http://www.esri.com*).

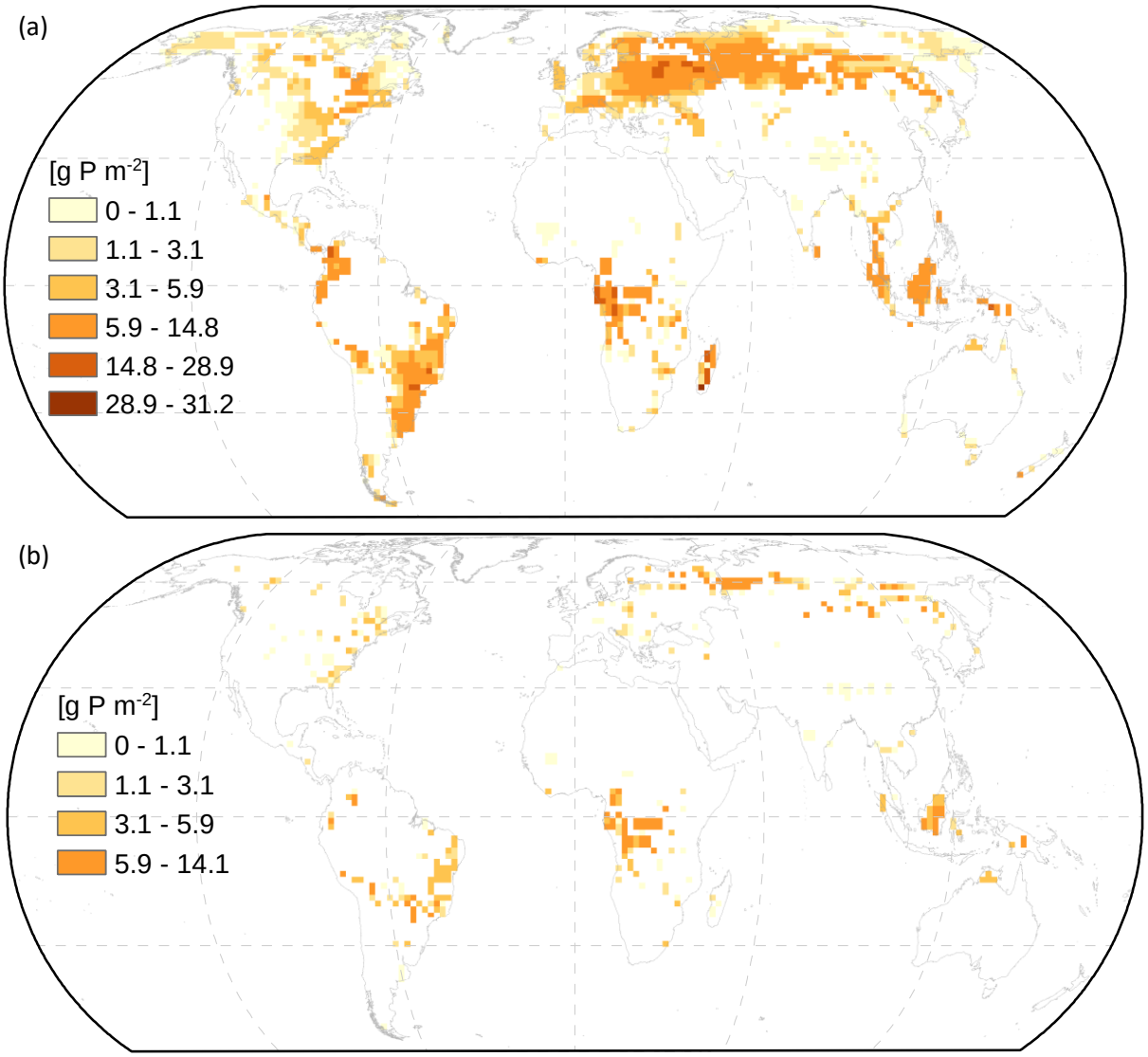

Fig. S9: Areas with a potential P gap for the nutrient budget of the N-unlimited AR scenario (after 94 years of simulation) assuming P concentrations within foliar and wood material corresponding to 95th percentile values (main text Table 1). a) Geogenic P supply scenario one (geogenic P from weathering plus atmospheric P deposition as source of P). b) Geogenic P supply scenario two (geogenic P from soil inorganic labile P and organic P pools plus atmospheric P deposition and P from weathering as source of P). Map generated with ESRI ArcGIS 10.6 (http://www.esri.com).

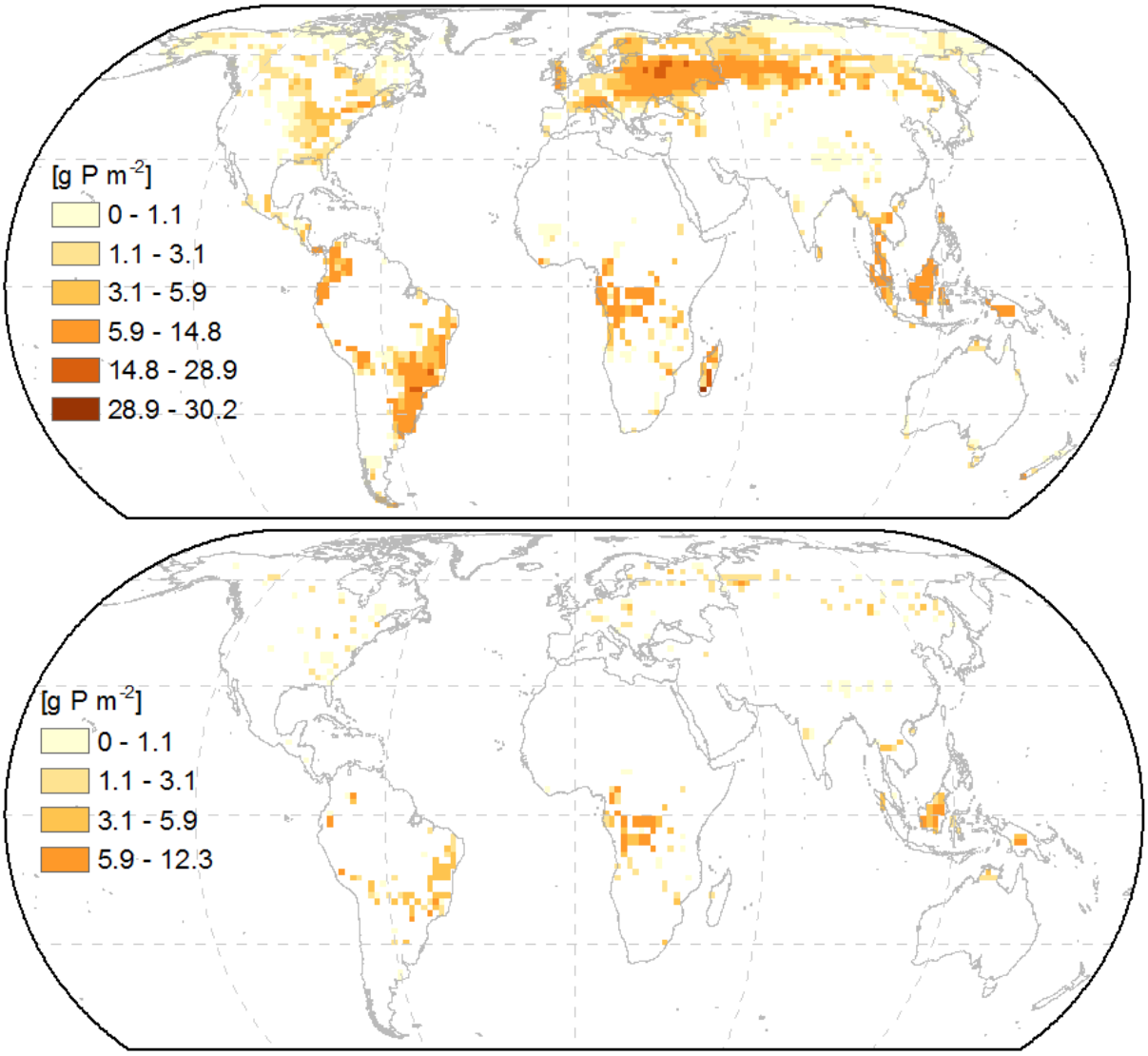

Fig. S10: Areas with a potential P gap for the nutrient budget of the N-limited AR scenario (after 94 years of simulation) assuming P concentrations within foliar and wood material corresponding to 95th values (main text Table 1). a) Geogenic P supply scenario one (geogenic P from weathering plus atmospheric P deposition as source of P). b) Geogenic P supply scenario two (geogenic P from soil inorganic labile P and organic P pools plus atmospheric P deposition and P from weathering as source of P). Map generated with ESRI ArcGIS 10.6 (http://www.esri.com).

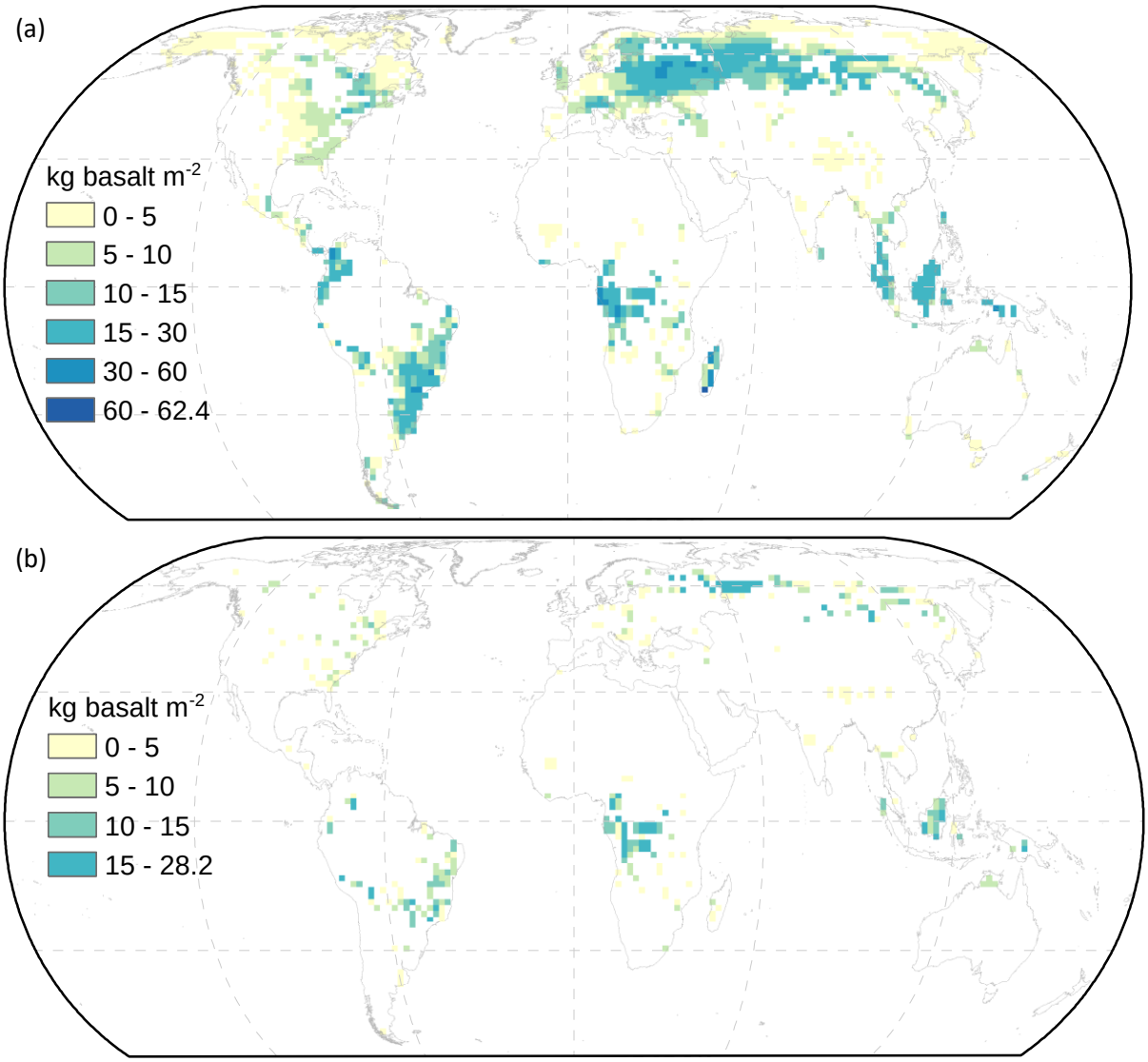

Fig. S11: Basalt deployment necessary to close P gaps from P budget scenarios of Fig. S9. a) Geogenic P supply scenario one (geogenic P from weathering plus atmospheric P deposition as source of P). b) Geogenic P supply scenario two (geogenic P from soil inorganic labile P and organic P pools plus atmospheric P deposition and P from weathering as source of P). Map generated with ESRI ArcGIS 10.6 (*http://www.esri.com*).

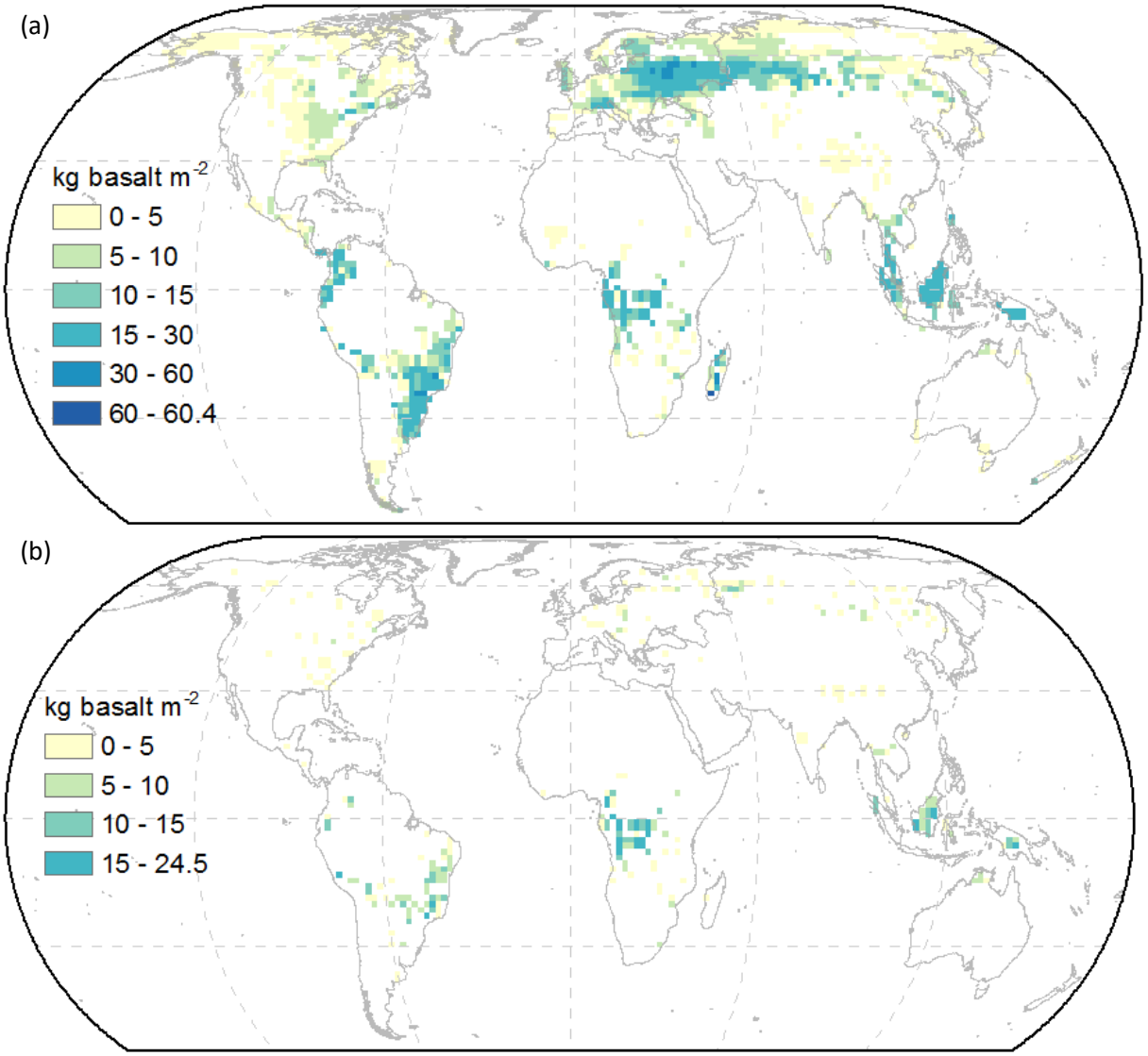

Fig. S12: Basalt deployment necessary to close P gaps from P budget scenarios of Fig. S10. a) Geogenic P supply scenario one (geogenic P from weathering plus atmospheric P deposition as source of P). b) Geogenic P supply scenario two (geogenic P from soil inorganic labile P and organic P pools plus atmospheric P deposition and P from weathering as source of P). Map generated with ESRI ArcGIS 10.6 (*http://www.esri.com*).

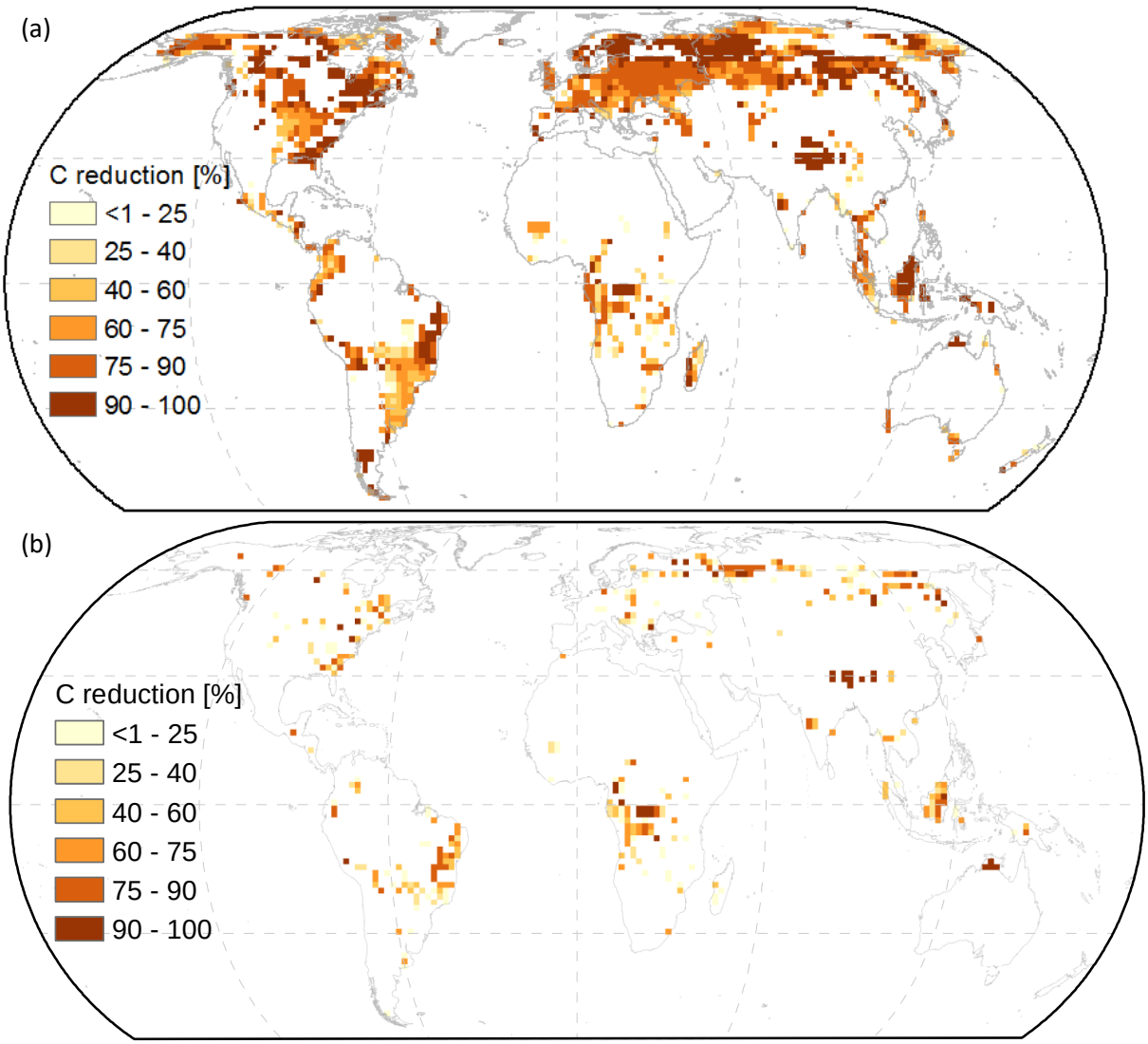

Fig. S13: Forest C sequestration reduction due to geogenic P limitation assuming P concentrations within foliar and wood material corresponding to 95th values (main text Table 1) estimated from stoichiometric C:P ratios. a) C-reduction based on P gaps of Fig. S9a, obtained for geogenic P supply scenario one (geogenic P from weathering plus atmospheric P deposition as source of P). b) C-reduction based on P gaps of Fig. S9b, obtained for geogenic P supply scenario two (geogenic P from soil inorganic labile P and organic P pools plus atmospheric P deposition and P from weathering as source of P). Map generated with ESRI ArcGIS 10.6 (*http://www.esri.com*).

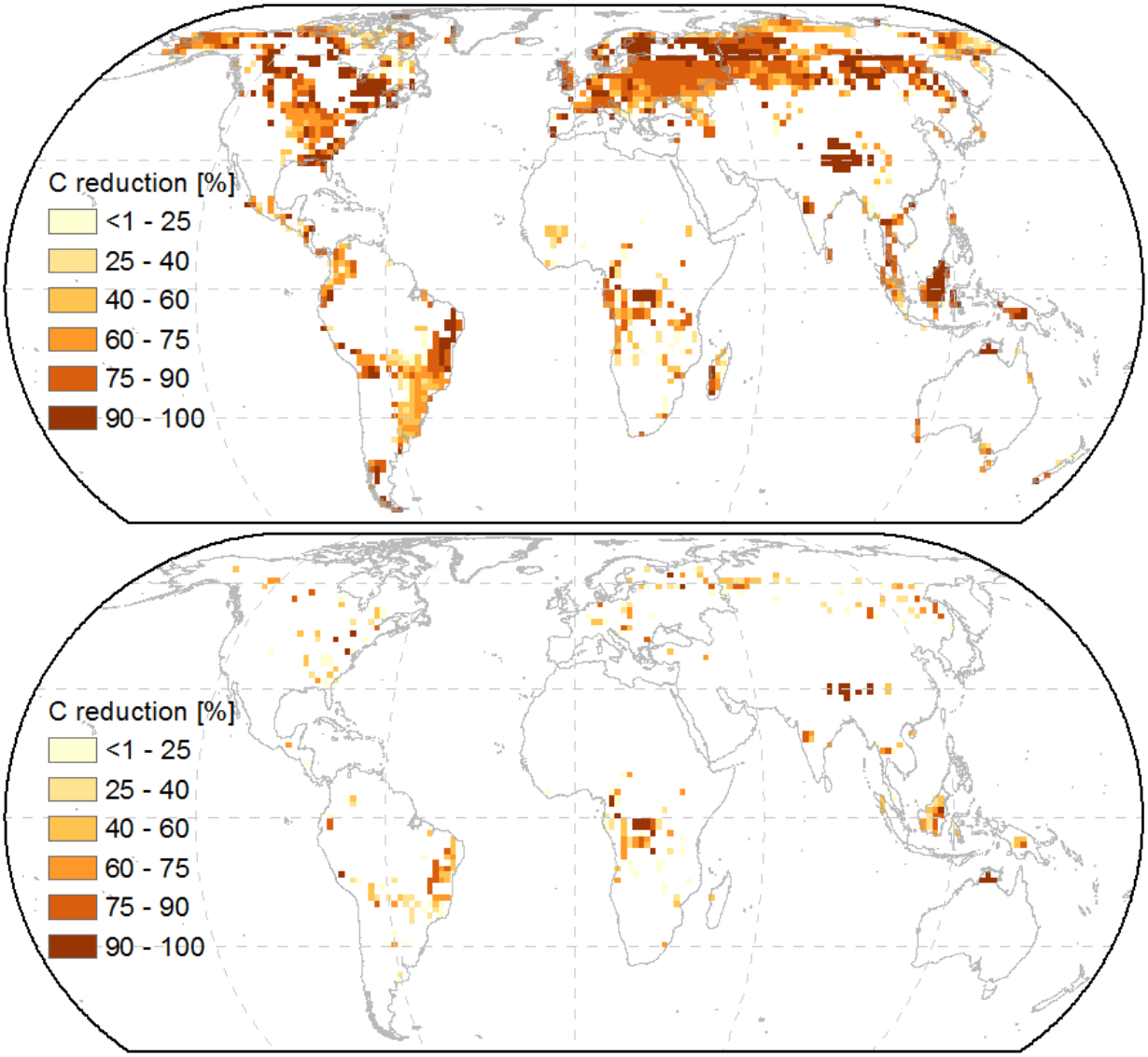

Fig. S14: Forest C sequestration reduction due to geogenic P limitation assuming P concentrations within foliar and wood material corresponding to 95th values (main text Table 1) estimated from stoichiometric C:P ratios. a) C-reduction based on P gaps of Fig. S10a, obtained for geogenic P supply scenario one (geogenic P from weathering plus atmospheric P deposition as source of P). b) C-reduction based on P gaps of Fig. S10b, obtained for geogenic P supply scenario two (geogenic P from soil inorganic labile P and organic P pools plus atmospheric P deposition and P from weathering as source of P). Map generated with ESRI ArcGIS 10.6 (*http://www.esri.com*).

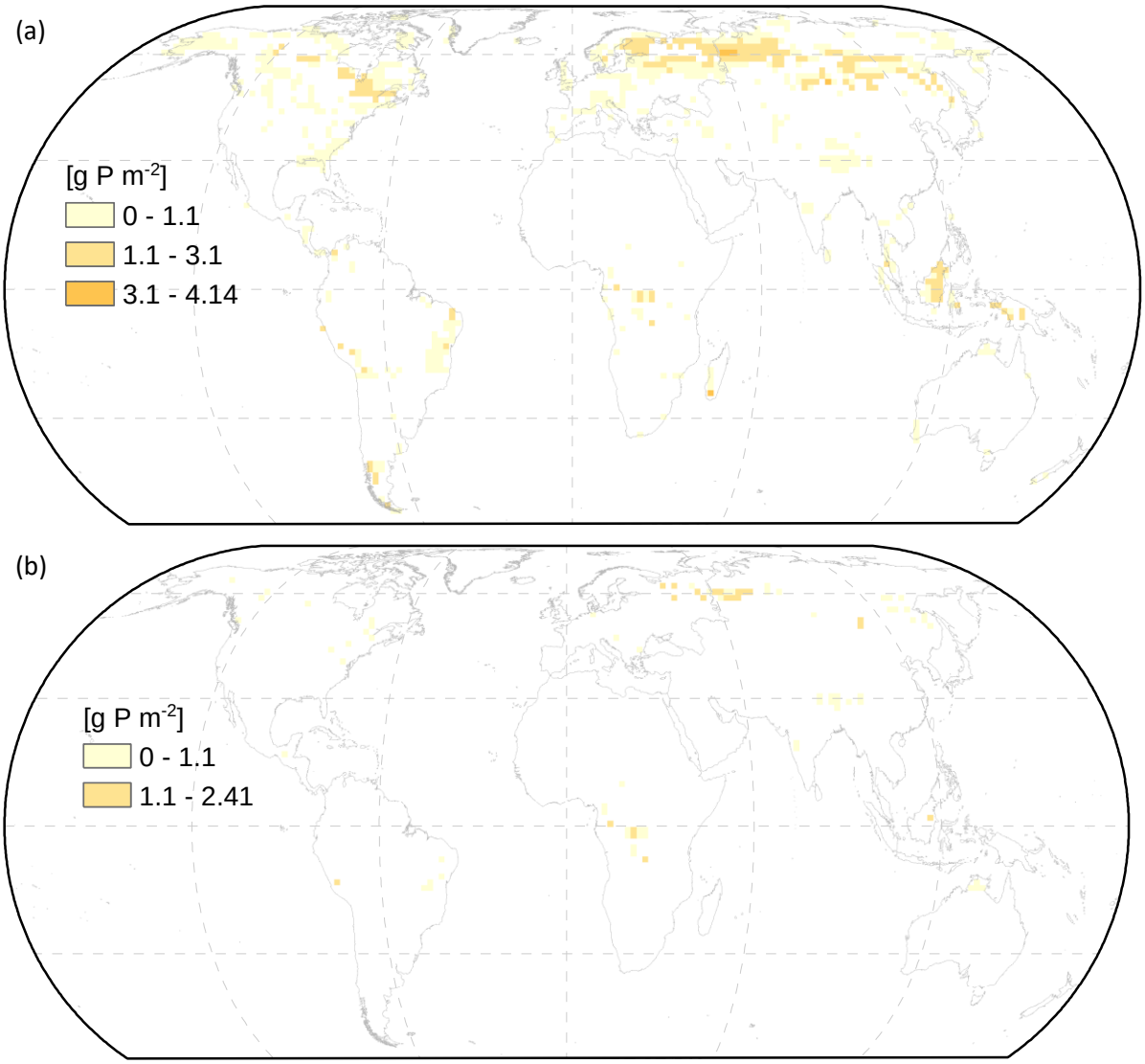

Fig. S15: Areas with a potential P gap for the nutrient budget of the N-unlimited AR scenario (after 94 years of simulation) assuming P concentrations within foliar and wood material corresponding to 5th values (main text Table 1). a) Geogenic P supply scenario one (geogenic P from weathering plus atmospheric P deposition as source of P). b) Geogenic P supply scenario two (geogenic P from soil inorganic labile P and organic P pools plus atmospheric P deposition and P from weathering as source of P). Map generated with ESRI ArcGIS 10.6 (http://www.esri.com).

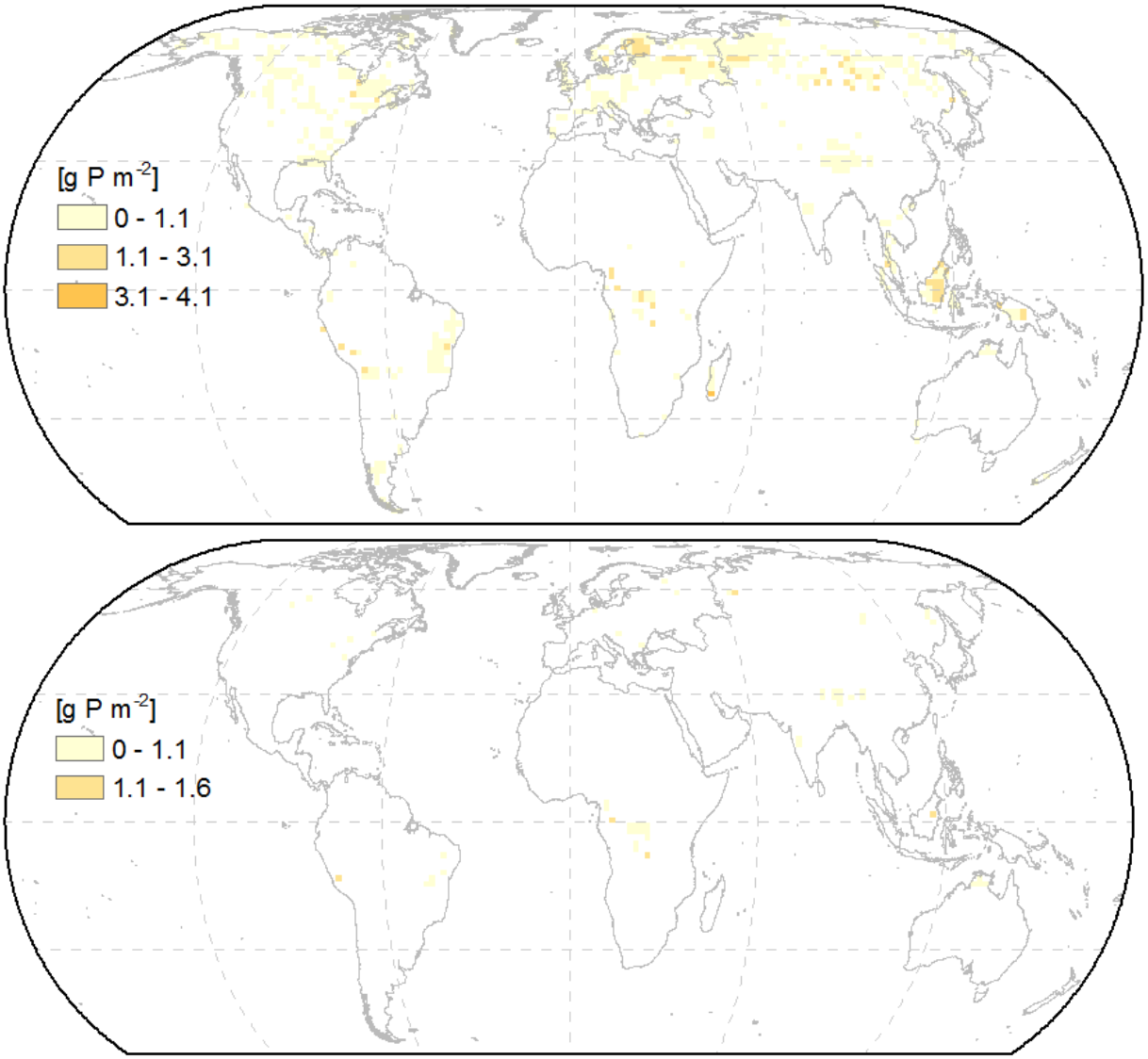

Fig. S16: Areas with a potential P gap for the nutrient budget of the N-limited AR scenario (after 94 years of simulation) assuming P concentrations within foliar and wood material corresponding to 5th values (main text Table 1). a) Geogenic P supply scenario one (geogenic P from weathering plus atmospheric P deposition as source of P). b) Geogenic P supply scenario two (geogenic P from soil inorganic labile P and organic P pools plus atmospheric P deposition and P from weathering as source of P). Map generated with ESRI ArcGIS 10.6 (http://www.esri.com).

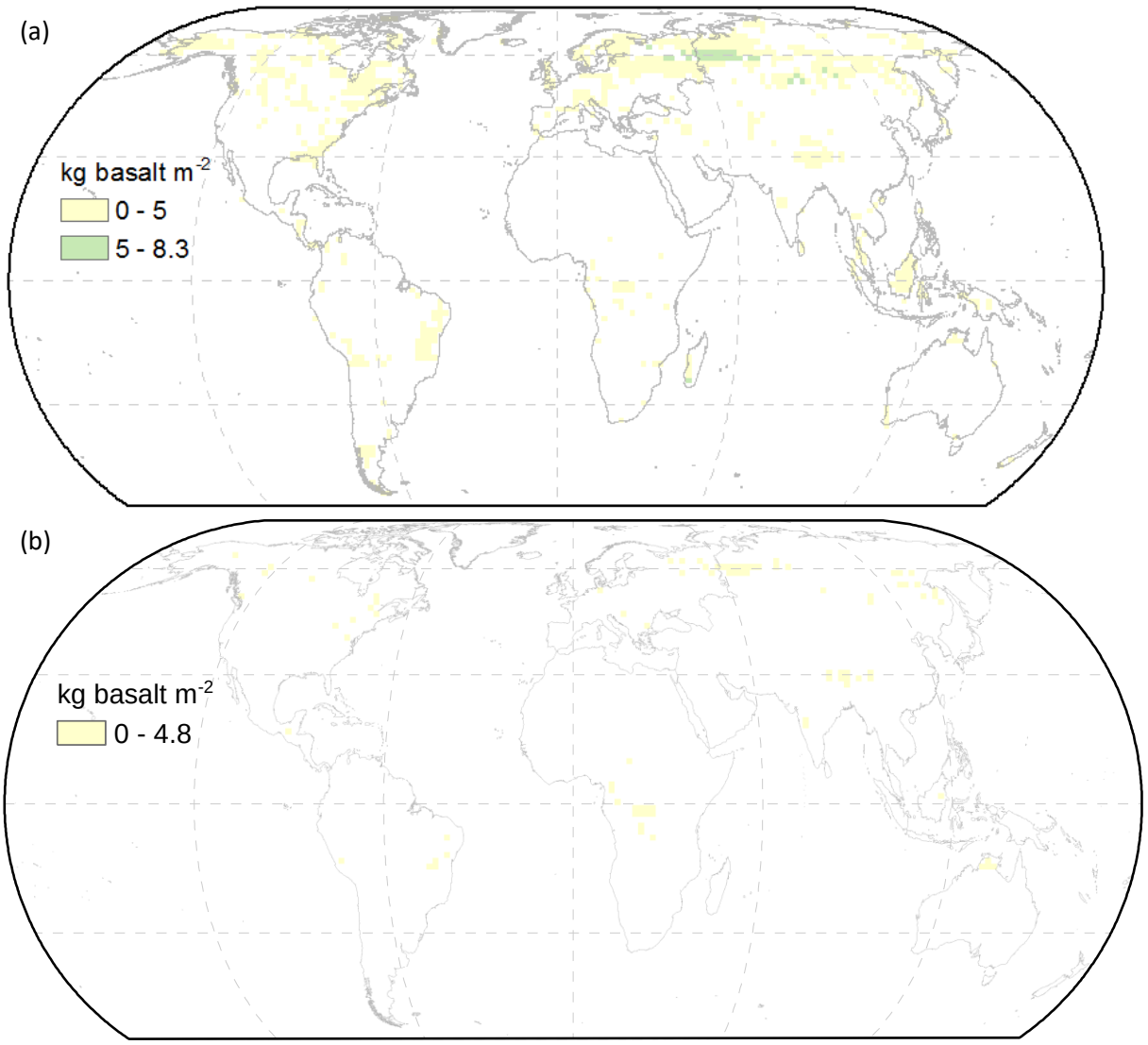

Fig. S17: Basalt deployment necessary to close P gaps from P budget scenarios of Fig. S15. a) Geogenic P supply scenario one (geogenic P from weathering plus atmospheric P deposition as source of P). b) Geogenic P supply scenario two (geogenic P from soil inorganic labile P and organic P pools plus atmospheric P deposition and P from weathering as source of P). Map generated with ESRI ArcGIS 10.6 (*http://www.esri.com*).

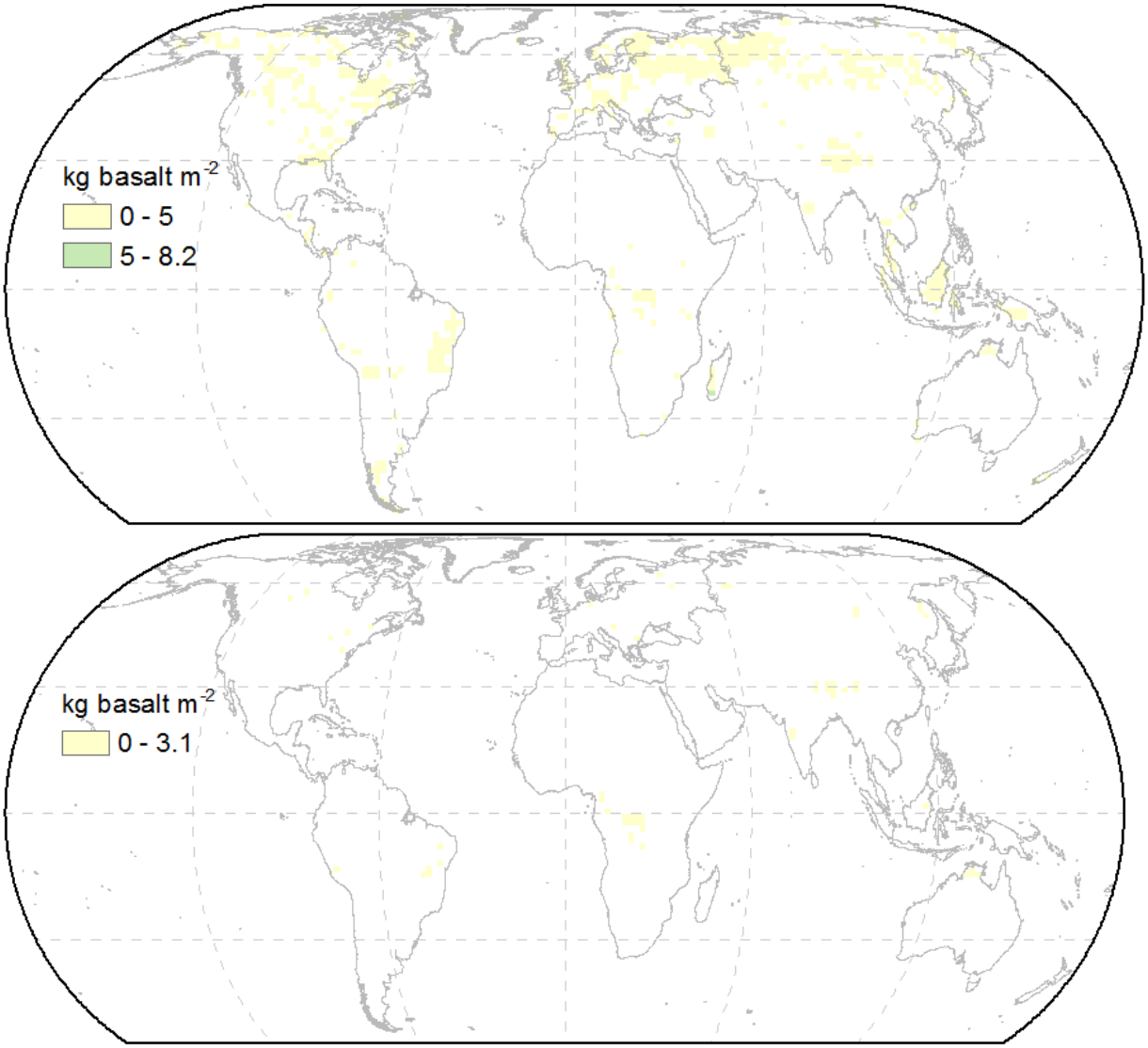

Fig. S18: Basalt deployment necessary to close P gaps from P budget scenarios of Fig. S16. a) Geogenic P supply scenario one (geogenic P from weathering plus atmospheric P deposition as source of P). b) Geogenic P supply scenario two (geogenic P from soil inorganic labile P and organic P pools plus atmospheric P deposition and P from weathering as source of P). Map generated with ESRI ArcGIS 10.6 (*http://www.esri.com*).

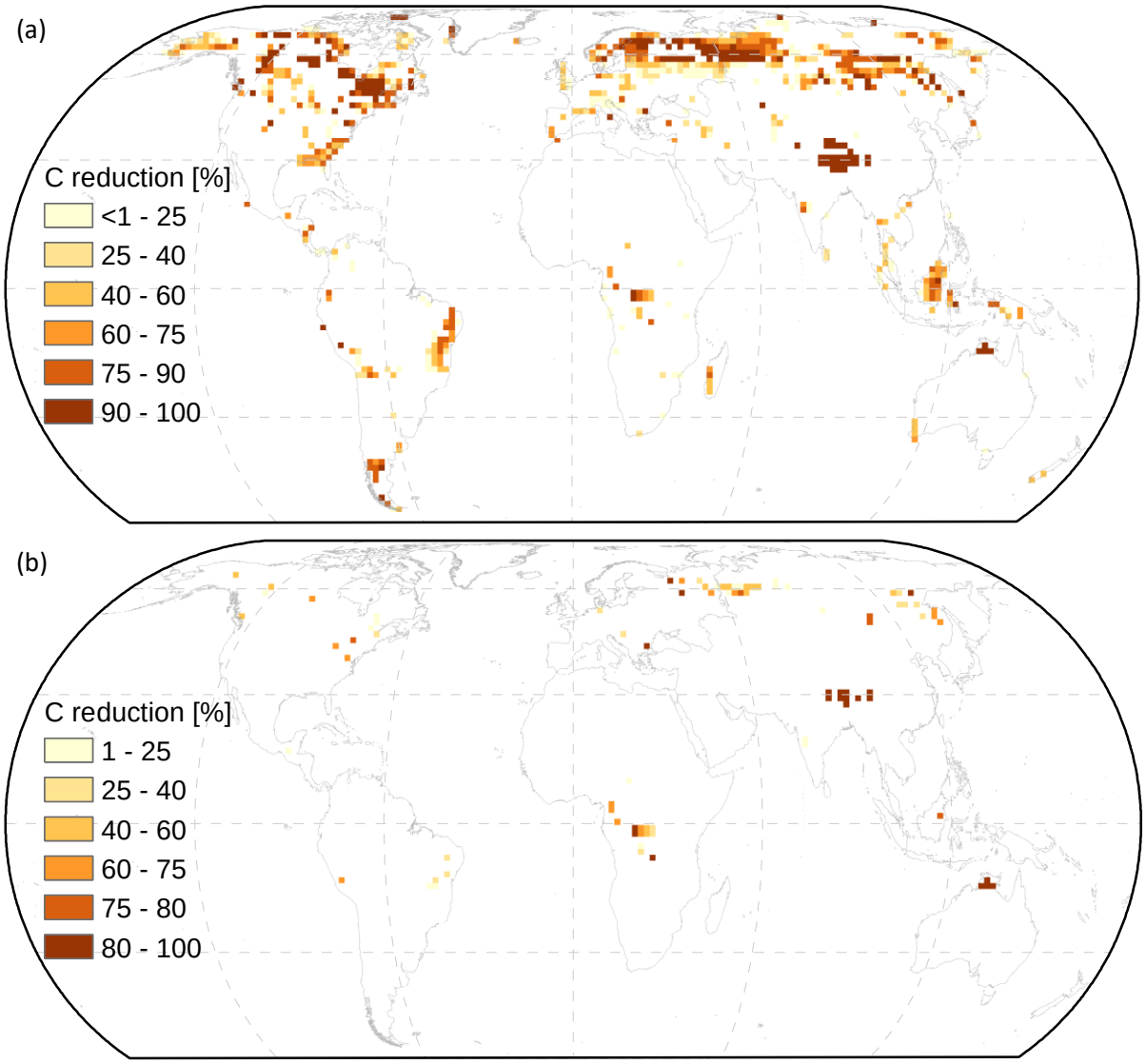

Fig. S19: Forest C sequestration reduction due to geogenic P limitation assuming P concentrations within foliar and wood material corresponding to 5th values (main text Table 1) estimated from stoichiometric C:P ratios. a) C-reduction based on P gaps of Fig. S15a, obtained for geogenic P supply scenario one (geogenic P from weathering plus atmospheric P deposition as source of P). b) C-reduction based on P gaps of Fig. S15b, obtained for geogenic P supply scenario two (geogenic P from soil inorganic labile P and organic P pools plus atmospheric P deposition and P from weathering as source of P). Map generated with ESRI ArcGIS 10.6 (*http://www.esri.com*).

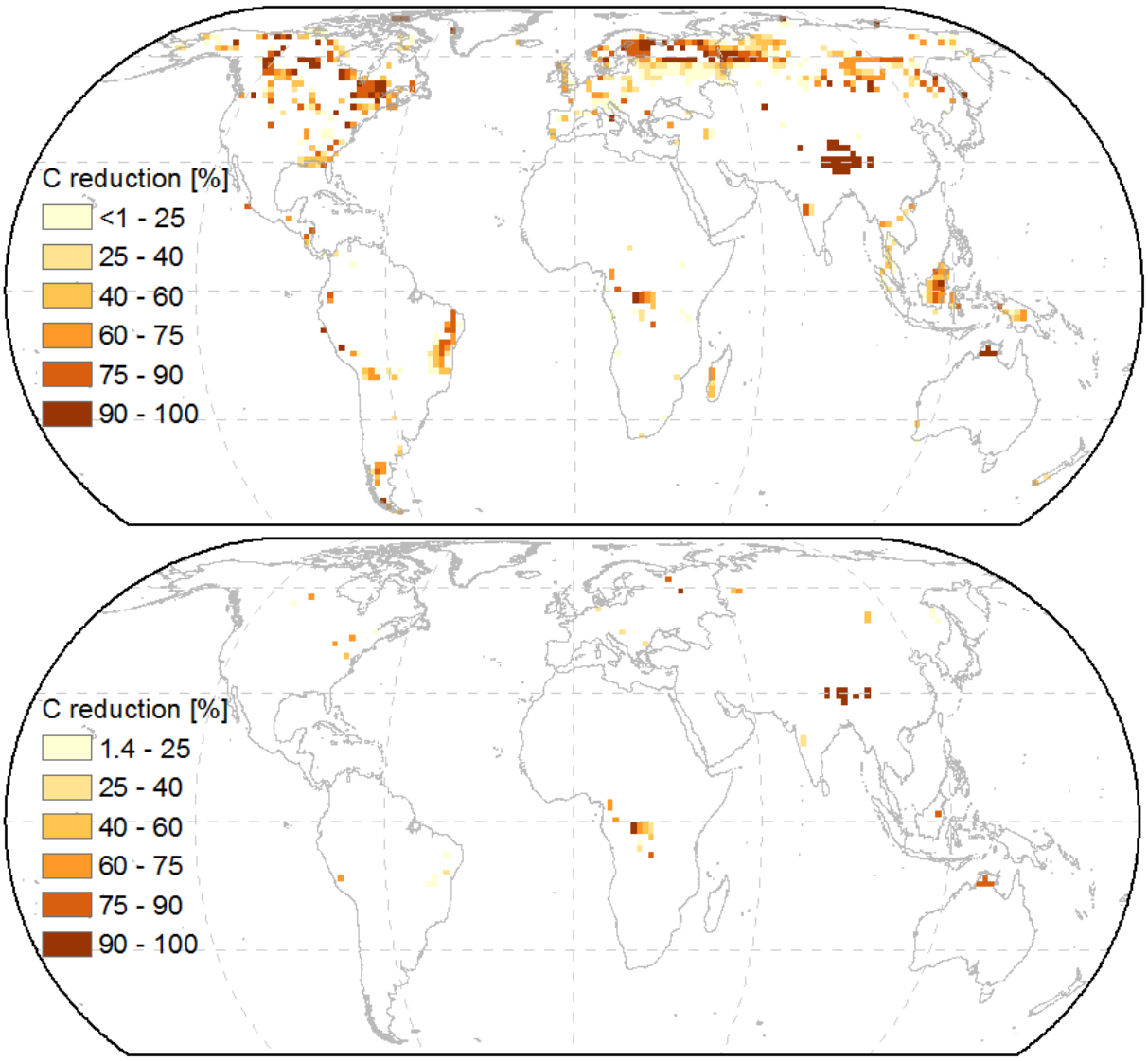

Fig. S20: Forest C sequestration reduction due to geogenic P limitation assuming P concentrations within foliar and wood material corresponding to 5th values (main text Table 1) estimated from stoichiometric C:P ratios. a) C-reduction based on P gaps of Fig. S16a, obtained for geogenic P supply scenario one (geogenic P from weathering plus atmospheric P deposition as source of P). b) C-reduction based on P gaps of Fig. S16b, obtained for geogenic P supply scenario two (geogenic P from soil inorganic labile P and organic P pools plus atmospheric P deposition and P from weathering as source of P). Map generated with ESRI ArcGIS 10.6 (*http://www.esri.com*).

The predicted C sequestration by N-unlimited AR scenario from Kracher (2017) is 2.4 Gt C a^{-1}. Different authors reported the potential C sequestration by afforestation or reforestation being of 0.3 – 3.3 Gt C a^{-1} for the end of 2100 (National Research Council, 2015;Lenton, 2014, 2010;Smith et al., 2015 apud Fuss et al., 2018).

The here estimated P demand based on the predicted biomass growth to sequester 224 Gt C (N-unlimited AR scenario) amounts to 244 Mt P on global scale for a mean wood and leaves P content. The potential C sequestration and the P demand of the N-unlimited AR scenario is higher than for the N-limited AR scenario. Based on global and US specific databases, the range of N stock-based additional P demand for the N-unlimited scenario is 88 / 417 Mt P; 5th / 95th percentile for wood and leaves chemistry.

The P budget for geogenic P supply scenario one, which considers P supply by weathering and atmospheric P deposition, for both N supply AR scenarios suggest that P deficiency areas are distributed along the world, but with higher occurrence within the northern hemisphere (Fig. S21a). However, for geogenic P supply scenario two, which is the same as geogenic P supply scenario one plus geogenic P from soil inorganic labile P and organic P pools, the P deficiency areas are predominantly located

at the southern hemisphere for both N supply AR scenarios (Fig. S21b). If P is the only limiting nutrient, it is expected a C reduction of 1.8 – 52% from the projected 224 Gt C, with mean C reduction of 39% for the geogenic P supply scenario one and 6% for the geogenic P supply scenario two (Table S2). If N and P are limiting nutrients, it is expected a C reduction of 16.5 – 59%, with mean C reduction of 47% for the geogenic P supply scenario one and 19% for the geogenic P supply scenario two. Accounting for N and P limitation on AR suggests that, in average; the biomass production will be affected, which decreases the C sequestration potential of AR strategies (Table S2). In some areas, the C sequestration reduction can reach up to 100% from predicted C sequestration of the AR models (Fig. S22).

Assuming a median P content of 500 ppm in basalt, *cf.*, Fig. S4 chapter S3, the maximum mass applied in 94 years would be of 34 and 13 kg basalt m^{-2} respectively for P gap from geogenic P supply scenarios one and two for the N-unlimited AR scenario (Fig. S8). A total amount of 3.6 – 454 Gt basalt (N-unlimited AR scenario) applied by EW would be needed to cover the projected P gaps. To reach the maximum projected C sequestration potential of AR, covering the N and P biomass demand would be necessary. Basalt has a carbon capture potential of ~0.3 tCO_2 t^{-1} basalt (Renforth, 2012), sequestering 1.08 – 136.2 Gt CO_2 by the end of 2100 if basalt powder would be deployed to cover P gaps of the N-unlimited AR scenario.

The nutrient concentration of rocks will influence the necessary amounts to cover P gap of each P budget scenario for the AR scenarios. The cumulative applied rock powder mass will be different for each rock type (Table S1), with basalt being more effective to supply P for the estimated P gap areas due to relative high P content.

For a chemical composition corresponding to the 95^{th} percentile, 10 kg basalt m^{-2} would cover the maximum projected P gaps for all P supply scenarios. For a median chemical composition, deploying 34 kg basalt m^{-2} would cover all the P gaps of the two geogenic P supply scenarios for the N-unlimited AR scenario and for the 5^{th} percentile the necessary amount of rock would get even higher (Table S1).

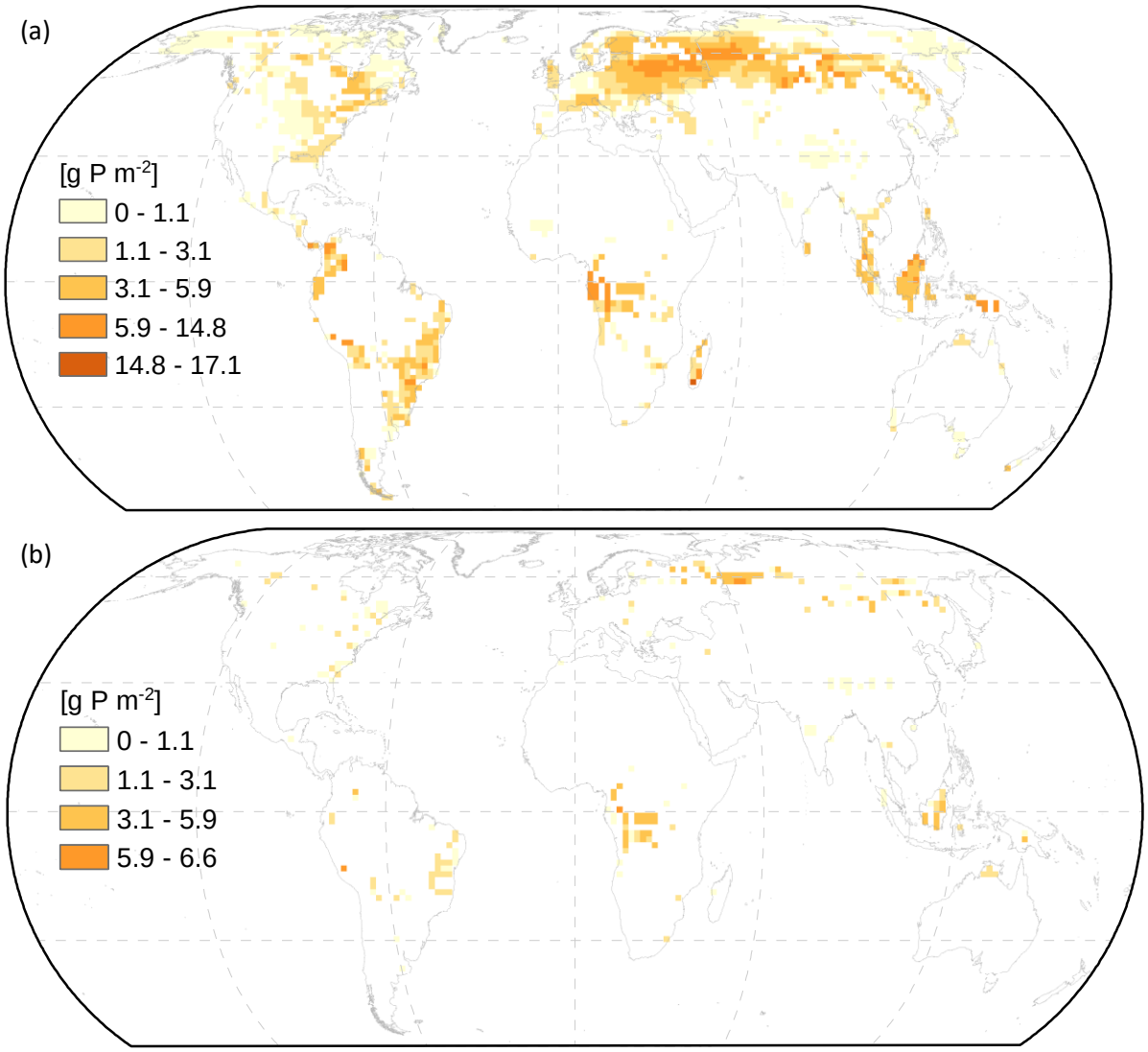

Fig. S21: Areas with potential P gap for the nutrient budget of the N-unlimited AR scenario (after 94 years of simulation) assuming P concentrations within foliar and wood material corresponding to mean values (Table 1 main text). a) Geogenic P supply scenario one (geogenic P from weathering plus atmospheric P deposition as source of P). b) Geogenic P supply scenario two (geogenic P from soil inorganic labile P and organic P pools plus atmospheric P deposition and P from weathering as source of P). Map generated with ESRI ArcGIS 10.6 (http://www.esri.com).

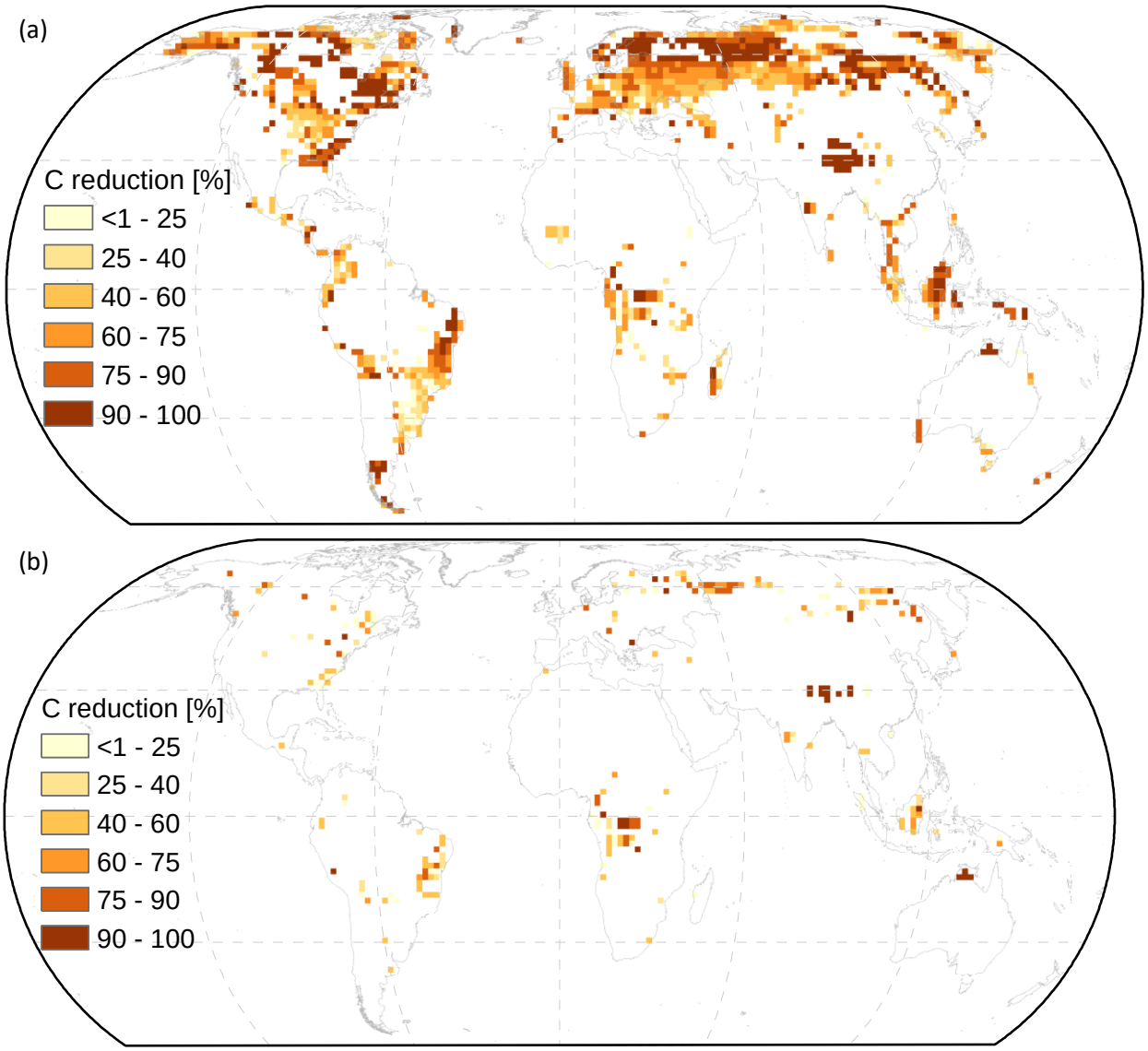

Fig. S22: Reduction on forest C sequestration due to geogenic P limitation. C-reduction estimated from stoichiometric C:P ratios for the N-unlimited AR scenario assuming P concentrations within foliar and wood material corresponding to mean values (Table 1 main text). a) C-reduction based on P gaps of Fig. S21a, obtained for geogenic P supply scenario one (geogenic P from weathering plus atmospheric P deposition as source of P). b) C-reduction based on P gaps of Fig. S21b, obtained for geogenic P supply scenario two (geogenic P from soil inorganic labile P and organic P pools plus atmospheric P deposition and P from weathering as source of P). For resulting global C reduction check Table S2. Map generated with ESRI ArcGIS 10.6 (http://www.esri.com).

Table S1: Rock powder application for a chemistry corresponding to the 5th percentile, assuming full rock dissolution, to cover maximum and median estimated P gaps for the N-unlimited AR scenario (minimum values can be neglected). For the potential macronutrient supply, see Fig. S6 and Fig. S7.

	P gap [g P m^{-2}]	Rhyolite	Dacite	Andesite	Basalt
		[kg rock m^{-2}]			
Scenario one	17.1	783.4	156.7	120.5	112.0
	2.1	19.0	6.3	6.0	3.8
Scenario two	6.6	302.6	60.5	46.5	43.2
	1.8	17.0	5.7	5.3	3.4

Table S2: Global P gap, maximum estimated P gap, maximum C sequestration reduction, and global C reduction for the natural N supply (N-limited) AR scenario (projected C sequestration of 190 Gt C) and for the N fertilization (N-unlimited) AR scenario (projected C sequestration of 224 Gt C).

N supply	Geogenic P supply	Maximum estimated P gap [g P m^{-2}]			Global P gap [Mt P]			Maximum C sequestration reduction [kg C m^{-2}]			Global C reduction [Gt C]		
		Wood and leaves P content											
		5th percentile	mean	95th percentile	5th percentile	mean	95th percentile	5th percentile	mean	95th percentile	5th percentile	mean	95th percentile
Unlimited	Scenario one	4.1	17.1	31.2	16.0	100.0	227.0	10.0	15.0	16.0	34.0	88.0	117.0
	Scenario two	2.4	6.6	14.1	1.8	15.0	49.0	4.6	6.1	7.6	4.0	13.0	25.0

S5. Impacts on soil hydrology

Pedotransfer functions (PTFs) are used to estimate soil hydraulic properties (Schaap et al., 2001;Whitfield and Reid, 2013;Wösten et al., 2001) and such approximations have proven to be a suitable approach (Vienken and Dietrich, 2011). PTFs make use of statistical analysis (Saxton and Rawls, 2006;Wösten et al., 2001), artificial neural networks and or other methods applied to large soil databases of measured data (Wösten et al., 2001). The equations from Saxton et al. (1986) performed the best estimations of soil hydraulic properties (Gijsman et al., 2002). Later on, Saxton and Rawls (2006) improved Saxton et al. (1986) PTFs. Therefore, potential changes in soil hydrology, due to the application of a fine basalt texture (15.6% clay, 83.8% silt, and 0.6% fine sand) or a coarse basalt texture (15.6% clay, 53.8% silt, and 30.6% fine sand) were estimated based on grain size distribution and organic matter fractions (Saxton and Rawls, 2006):

$$\theta_{1500} = \theta_{1500t} + (0.14 \times \theta_{1500t} - 0.02), \quad \text{(S1)}$$

$$\theta_{33} = \theta_{33t} + (1.283 \times (\theta_{33t})^2 - 0.374 \times (\theta_{33t}) - 0.015), \quad \text{(S2)}$$

$$\theta_{(S-33)} = \theta_{(S-33)t} + (0.636 \times \theta_{(S-33)t} - 0.107), \quad \text{(S3)}$$

$$\theta_S = \theta_{33} + \theta_{(S-33)} - 0.097 \times S + 0.043, \quad \text{(S4)}$$

$$K_S = 1930 \times (\theta_S - \theta_{33})^{(3-\lambda)}, \quad \text{(S5)}$$

with:

$$\theta_{1500t} = -0.024 \times S + 0.487 \times C + 0.006 \times OM + 0.005 \times (S \times OM) - 0.013(C \times OM) + 0.068(S \times C) + 0.031, \quad \text{(S6)}$$

$$\theta_{33t} = -0.251 \times S + 0.195 \times C + 0.011 \times OM + 0.006 \times (S \times OM) - 0.027 \times (C \times OM) + 0.452(S \times C) + 0.299, \quad \text{(S7)}$$

$$\theta_{(S-33)t} = 0.278 \times S + 0.034 \times C + 0.022 \times OM - 0.018 \times (S \times OM) - 0.027 \times (C \times OM) - 0.584 \times (S \times C) + 0.078, \quad \text{(S8)}$$

$$\lambda = [\frac{\ln(1500) - \ln(33)}{\ln(\theta_{33}) - \ln(\theta_{1500})}]^{-1}, \quad \text{(S9)}$$

where S and C respectively represent the soil texture corresponding to sand and clay diameters [wt %], OM is the soil organic matter [wt %], the moisture [wt %] are estimated by θ_{1500} and θ_{33} respectively representing the soil moisture for a pressure head of -1500 kPa (R^2 = 0.86) and of -33 kPa (R^2 = 0.63). $\theta_{(S-33)}$ and θ_S respectively corresponds to the 0 kPa to -33 kPa moisture (R^2 = 0.36), and to the saturated (0 kPa) moisture (R^2 < 0.25). K_S [mm h^{-1}] represents the saturated soil hydraulic conductivity and λ is the slope of the logarithmic tension-moisture curve. The plant available water is given by the difference between water content at a pressure head of -33 kPa and -1500 kPa (Saxton and Rawls, 2006).

The initial hydrologic properties of topsoil were estimated for a depth of 0.3 m, as it is the average depth usual machinery can homogeneously mix topsoil. Greater depths can be reached but under higher energy and labor costs (Fageria and Baligar, 2008). The global data set of derived soil properties (Batjes, 2005), which had textural information (sand, silt, and clay content) for shallow soil depths (0.3 m) was used. The raster had a resolution of 0.5° and the soil properties for the interest areas of biomass growth limitation (main text Fig. 2) were included by a spatial join (using Esri ArcMap 10.6). The nutrient deficient areas encompass soils of different textures and organic matter content, which had their initial K_S estimated separately based on eq. S5. The sum of clay, silt, and sand fractions within each cell should always be one, and were corrected when necessary:

$$G_{cor} = \frac{(G_{ini} \times M_{soil\_cell})}{\sum(G_{ini} \times M_{soil\_cell})}, \quad \text{(S10)}$$

with:

$$M_{soil\_cell} = V_{cell} \times \rho_{bulk\_cell}, \quad \text{(S11)}$$

where G_{ini} represents the initial topsoil texture of a specific raster cell [-]. V_{cell} [km^3] is the raster cell volume obtained by multiplying the area [km^2] to the soil depth of 0.3×10^{-3} km. ρ_{bulk_cell} is the raster cell topsoil bulk density [kg km^{-3}]. M_{soil_cell} is the total sediment mass of a raster cell [kg]. G_{cor} is the corrected soil texture [-].

The necessary rock powder mass was estimated based on cumulative P gaps ($M_{b_{cell}}$) obtained from the P budget that considered the natural P pools and P demand of afforestation. The impact of basalt powder application in soil K_S and PAW was estimated by assuming a homogeneous mixture between applied basalt powder and topsoil.

Basalt organic matter content is zero and basalt powder application on soil can potentially change its texture and soil organic matter (SOM) content. The changes were quantified by the initial SOM mass within a raster grid-cell normalized to the sum of applied basalt mass, mass of soil, and initial SOM mass:

$$OM_c = \frac{OM_{cell}}{M_{b\_cell} + M_{soil\_cell} + OM_{cell}} \times 100, \quad \text{(S12)}$$

with:

$$OM_{cell} = OM_{wt\%} \times M_{soil\_cell}, \quad \text{(S13)}$$

where OM_c is the corrected organic matter content [wt %], OM_{cell} is the organic matter mass within the raster cell [kg]. M_{b_cell} and M_{soil_cell}, both in [kg], are the mass of basalt and mass of soil for a specific raster cell.

The impacts in soil texture by rock powder application considered the textures of applied basalt mass added to the initial soil mass. It was assumed a content of 15.6% clay, 83.8% silt, and 0.6% fine sand for fine basalt powder and 15.6% clay, 53.8% silt, and 30.6% fine sand for a coarse basalt powder.

$$G_{bs} = \frac{\left(G_{ini} \times M_{sed_{cell}} + M_{b_{cell}} \times G_{basalt}\right)}{\Sigma\left(G_{ini} \times M_{sed_{cell}} + M_{b_{cell}} \times G_{basalt}\right)}, \quad \text{(S14)}$$

where G_{basalt} corresponds to the texture fractions of the fine or coarse basalt powder. G_{bs} corresponds to the texture fractions of resulting mixture of basalt plus soil.

Besides texture and organic matter, intrinsic grain properties, *e.g.*, the shape of grains and pores, tortuosity, specific surface area, and porosity, should be considered (Bear, 1972). The equations from Beyer (1964) are based on the non-uniformity of grain size distribution and density of the grain packing to estimate soil properties. Carrier III (2003) uses information on the particle grain size distribution, the particle shape, and the void ratio on his equations to estimate soil properties. However, such detailed information on a global scale is missing turning Beyer (1964) and Carrier III (2003) equations useless.

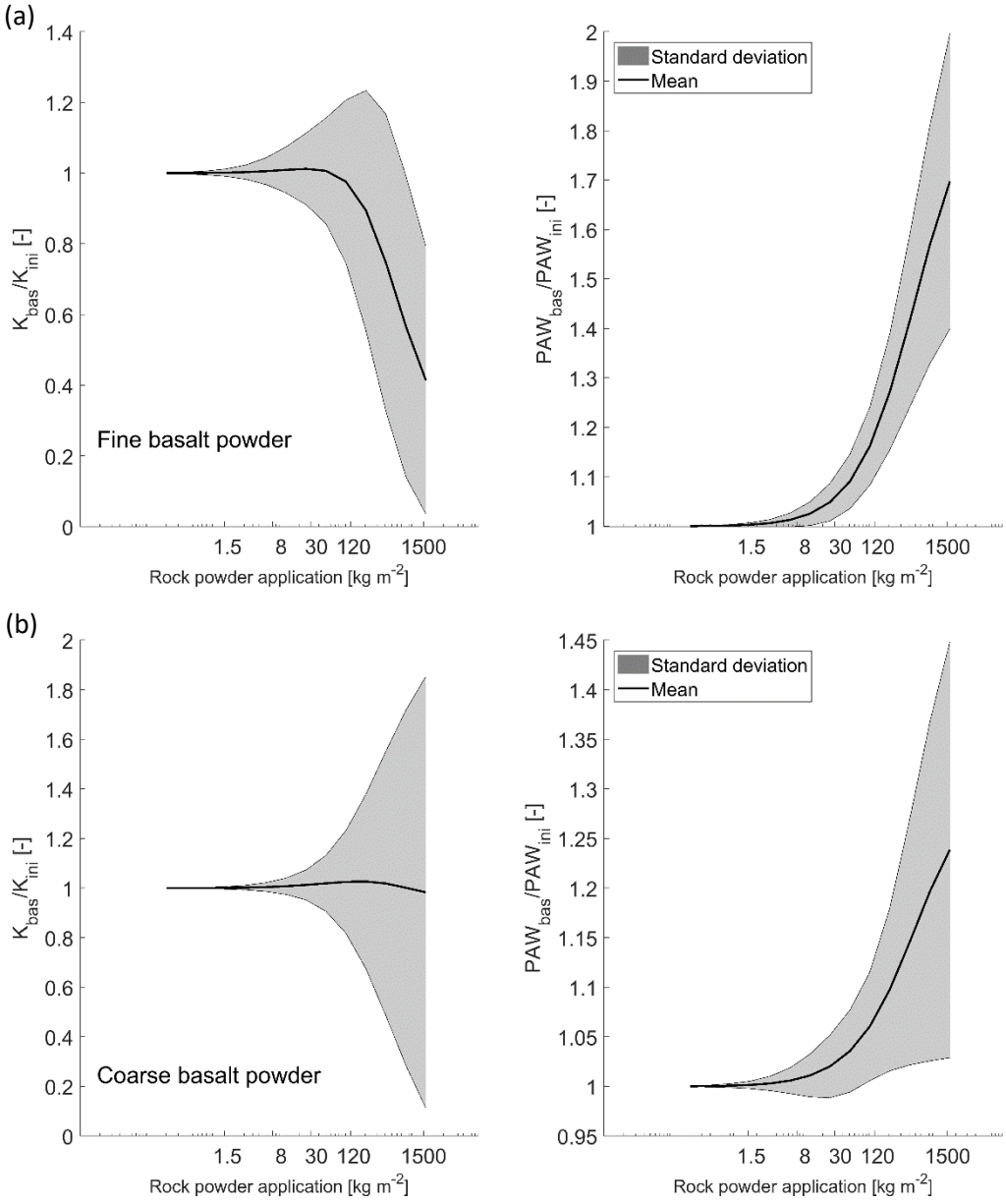

Fig. S23: Relative impacts on soil saturated hydraulic conductivity (K_S) and Plant Available Water (PAW). K_{bas} and PAW_{bas} respectively represents the estimated soil K_S and PAW after basalt application. K_{ini} is the estimated initial soil K_S and PAW_{ini} is the estimated initial PAW of different soils. a) Application of a fine basalt texture (15.6% clay, 83.8% silt, and 0.6% fine sand). b)

Application of a coarse basalt texture (15.6% clay, 53.8% silt, and 30.6% fine sand) for areas corresponding to P budget scenario two (main text Fig. 2b). Mean and standard deviations for n=2521 grid cells.

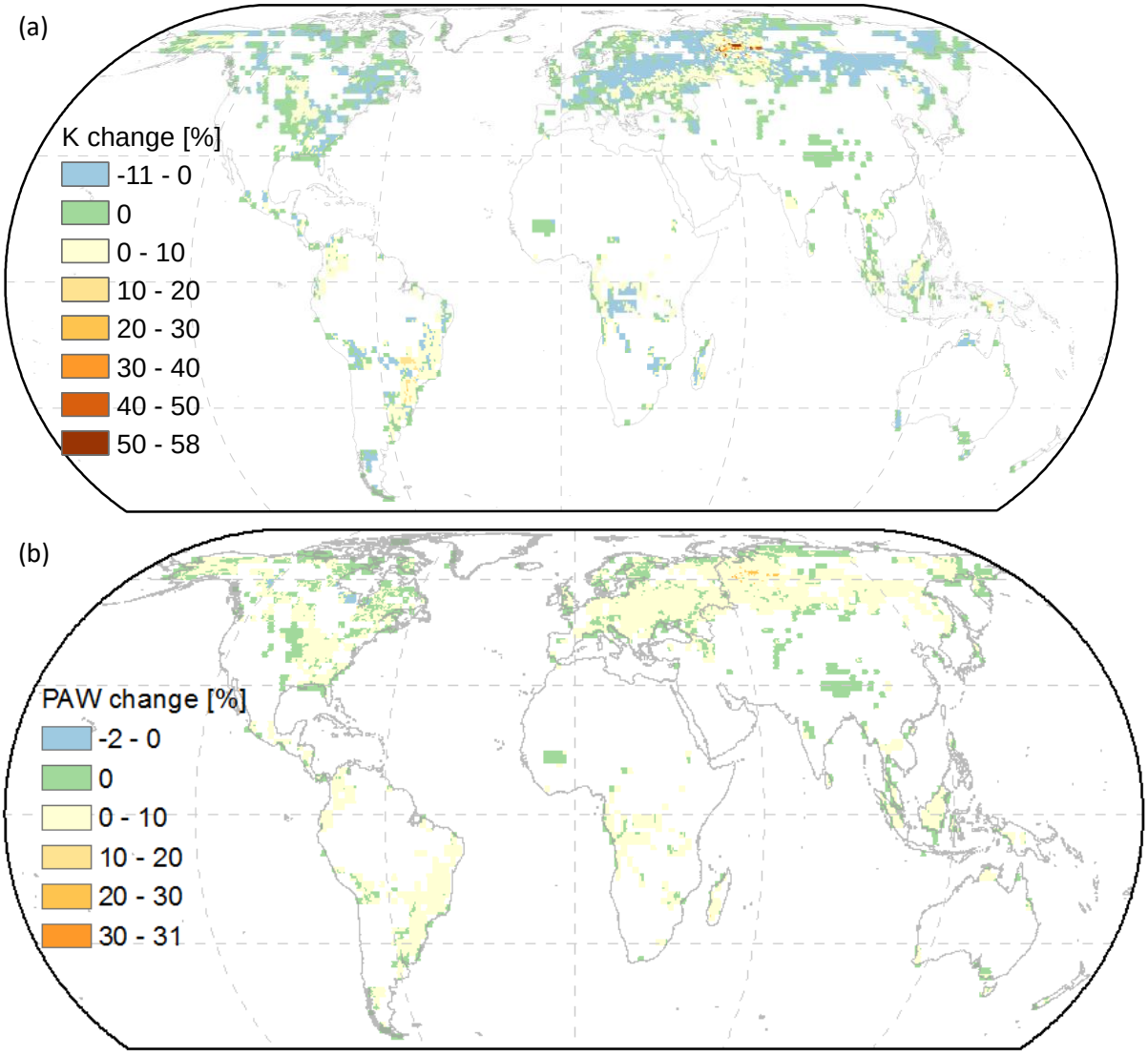

Fig. S24: Impacts on soil hydrology for basalt deployment mass coincident to Fig. S7a for a fine basalt texture (15.6% clay, 83.8% silt, and 0.6% sand) being deployed. a) Hydraulic conductivity (K) changes relative to initial soil values estimated according to Saxton and Rawls (2006) equations. b) Plant available water (PAW) changes relative to initial soil values estimated according to Saxton and Rawls (2006) equations. Map generated with ESRI ArcGIS 10.6 (*http://www.esri.com*).

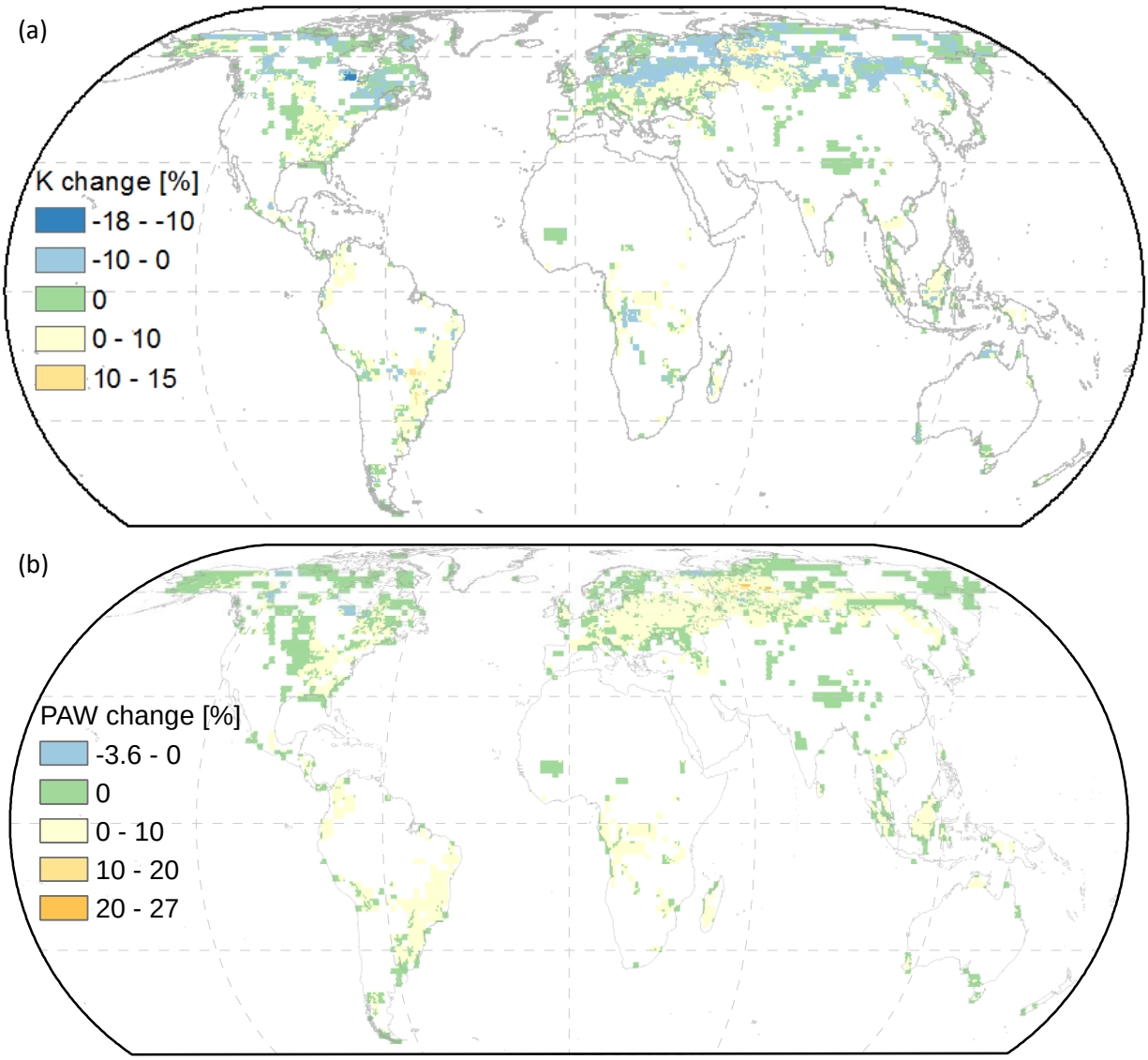

Fig. S25: Impacts on soil hydrology for basalt deployment mass coincident to Fig. S7a for a coarse basalt texture (15.6% clay, 53.8% silt, and 30.6% fine sand) being deployed. a) Hydraulic conductivity (K) changes relative to initial soil values estimated according to Saxton and Rawls (2006) equations. b) Plant available water (PAW) changes relative to initial soil values estimated according to Saxton and Rawls (2006) equations. Map generated with ESRI ArcGIS 10.6 (*http://www.esri.com*).

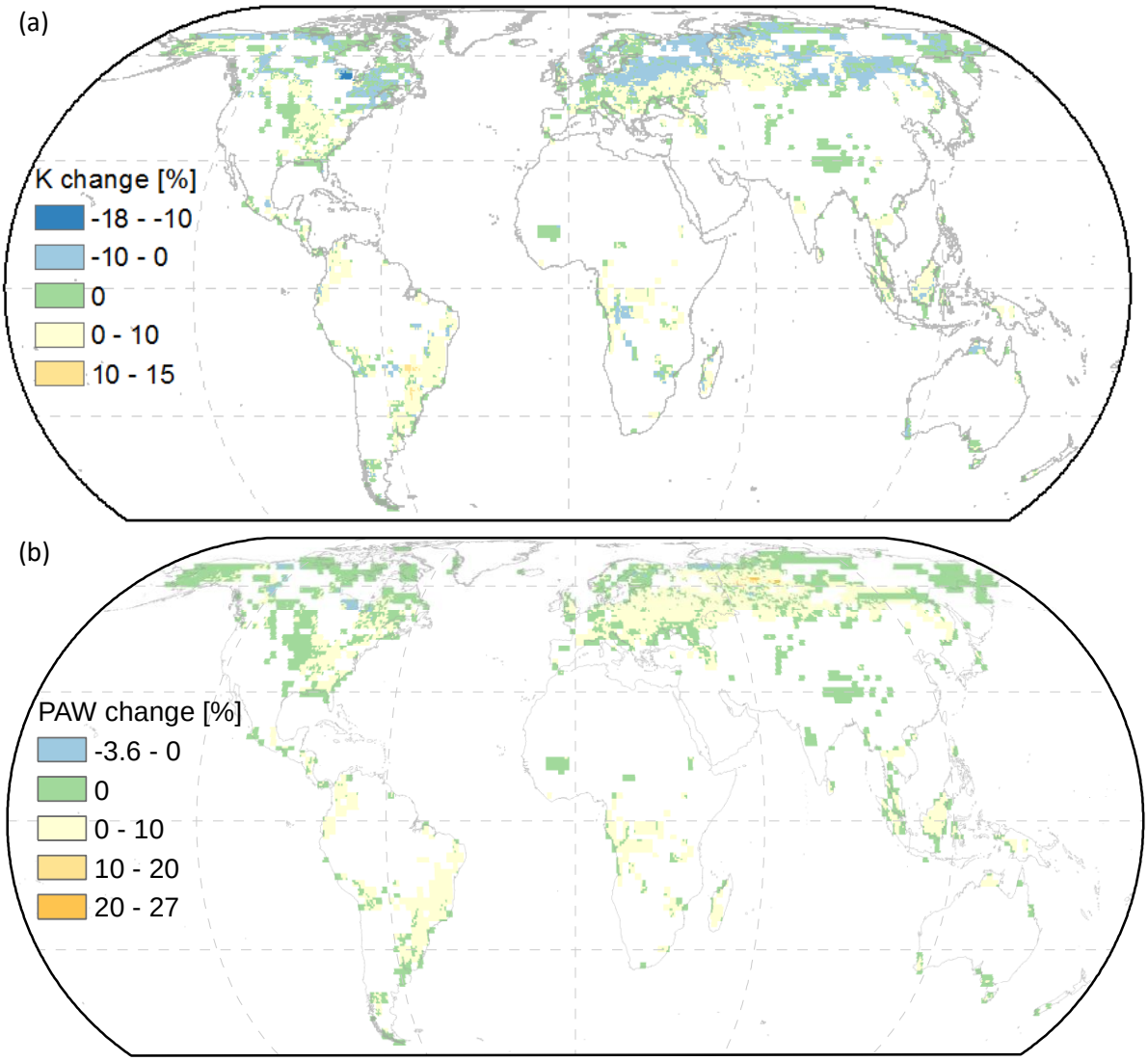

Fig. S26: Impacts on soil hydrology for basalt deployment mass coincident to Fig. S7b for a fine basalt texture (15.6% clay, 83.8% silt, and 0.6% sand) being deployed. a) Hydraulic conductivity (K) changes relative to initial soil values estimated according to Saxton and Rawls (2006) equations. b) Plant available water (PAW) changes relative to initial soil values estimated according to Saxton and Rawls (2006) equations. Map generated with ESRI ArcGIS 10.6 (*http://www.esri.com*).

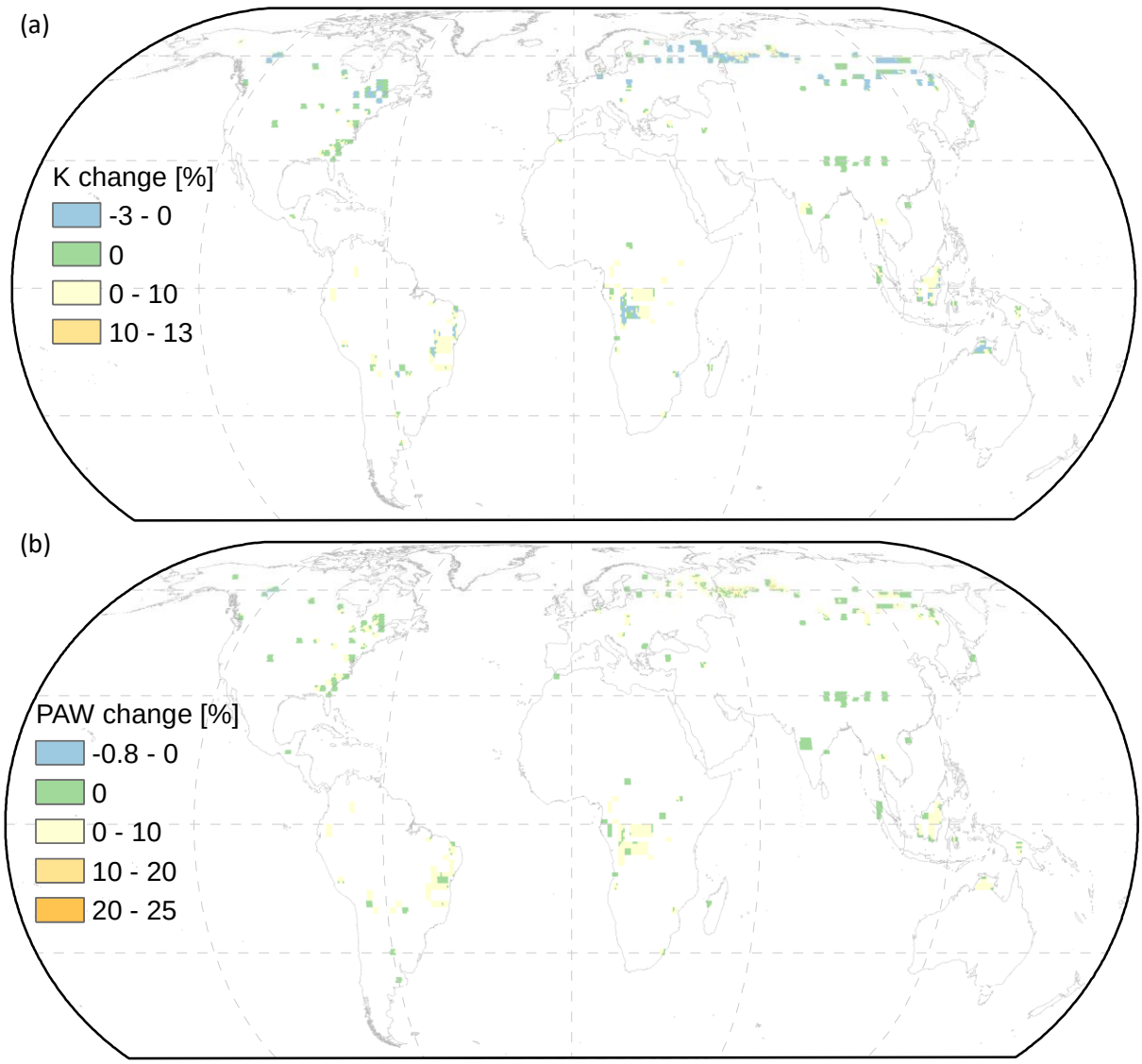

Fig. S27: Impacts on soil hydrology for basalt deployment mass coincident to Fig. S7b for a coarse basalt texture (15.6% clay, 53.8% silt, and 30.6% fine sand) being deployed. a) Hydraulic conductivity (K) changes relative to initial soil values estimated according to Saxton and Rawls (2006) equations. b) Plant available water (PAW) changes relative to initial soil values estimated according to Saxton and Rawls (2006) equations. Map generated with ESRI ArcGIS 10.6 (*http://www.esri.com*).

S6. References

Batjes, N.: ISRIC-WISE global data set of derived soil properties on a 0.5 by 0.5 degree grid (version 3.0), ISRIC – World Soil Information, 2005.

Bear, J.: Dynamics of fluids in porous media, American Elsevier., New York, 1972.

Beyer, W.: Zur bestimmung der wasserdurchlässigkeit von kiesen und sanden aus der kornverteilungskurve, WWT, 14, 165-168, 1964.

Carrier III, W. D.: Goodbye, hazen; hello, kozeny-carman, Journal of geotechnical and geoenvironmental engineering, 129, 1054-1056, 2003.

Council, N. R.: Climate Intervention: Carbon Dioxide Removal and Reliable Sequestration, The National Academies Press, Washington, DC, 154 pp., 2015.

Fageria, N. K., and Baligar, V. C.: Chapter 7 Ameliorating Soil Acidity of Tropical Oxisols by Liming For Sustainable Crop Production, in: Advances in Agronomy, Academic Press, 345-399, 2008.

Gijsman, A. J., Jagtap, S. S., and Jones, J. W.: Wading through a swamp of complete confusion: how to choose a method for estimating soil water retention parameters for crop models, European Journal of Agronomy, 18, 77-106, https://doi.org/10.1016/S1161-0301(02)00098-9, 2002.

Goll, D. S., Moosdorf, N., Hartmann, J., and Brovkin, V.: Climate-driven changes in chemical weathering and associated phosphorus release since 1850: Implications for the land carbon balance, Geophysical Research Letters, 41, 3553-3558, doi:10.1002/2014GL059471, 2014.

Hartmann, J., Moosdorf, N., Lauerwald, R., Hinderer, M., and West, A. J.: Global chemical weathering and associated P-release - The role of lithology, temperature and soil properties, Chemical Geology, 363, 145-163, 10.1016/j.chemgeo.2013.10.025, 2014.

Kracher, D.: Nitrogen-Related Constraints of Carbon Uptake by Large-Scale Forest Expansion: Simulation Study for Climate Change and Management Scenarios, Earth's Future, 5, 1102-1118, 10.1002/2017EF000622, 2017.

Lenton, T. M.: The potential for land-based biological CO2 removal to lower future atmospheric CO2 concentration, Carbon Management, 1, 145-160, 2010.

Lenton, T. M.: The global potential for carbon dioxide removal, Geoengineering of the Climate System, 52-79, 2014.

Renforth, P.: The potential of enhanced weathering in the UK, International Journal of Greenhouse Gas Control, 10, 229-243, 10.1016/j.ijggc.2012.06.011, 2012.

Saxton, K., Rawls, W. J., Romberger, J., and Papendick, R.: Estimating generalized soil-water characteristics from texture 1, Soil Science Society of America Journal, 50, 1031-1036, 1986.

Saxton, K. E., and Rawls, W. J.: Soil water characteristic estimates by texture and organic matter for hydrologic solutions, Soil science society of America Journal, 70, 1569-1578, 2006.

Schaap, M. G., Leij, F. J., and van Genuchten, M. T.: rosetta: a computer program for estimating soil hydraulic parameters with hierarchical pedotransfer functions, Journal of Hydrology, 251, 163-176, https://doi.org/10.1016/S0022-1694(01)00466-8, 2001.

Smith, P., Davis, S. J., Creutzig, F., Fuss, S., Minx, J., Gabrielle, B., Kato, E., Jackson, R. B., Cowie, A., Kriegler, E., van Vuuren, D. P., Rogelj, J., Ciais, P., Milne, J., Canadell, J. G., McCollum, D., Peters, G., Andrew, R., Krey, V., Shrestha, G., Friedlingstein, P., Gasser, T., Grübler, A., Heidug, W. K., Jonas, M., Jones, C. D., Kraxner, F., Littleton, E., Lowe, J., Moreira, J. R., Nakicenovic, N., Obersteiner, M., Patwardhan, A., Rogner, M., Rubin, E., Sharifi, A., Torvanger, A., Yamagata, Y., Edmonds, J., and Yongsung, C.: Biophysical and economic limits to negative CO2 emissions, Nature Climate Change, 6, 42, 10.1038/nclimate2870 https://www.nature.com/articles/nclimate2870#supplementary-information, 2015.

Vienken, T., and Dietrich, P.: Field evaluation of methods for determining hydraulic conductivity from grain size data, Journal of Hydrology, 400, 58-71, 2011.

Wang, R., Goll, D., Balkanski, Y., Hauglustaine, D., Boucher, O., Ciais, P., Janssens, I., Penuelas, J., Guenet, B., Sardans, J., Bopp, L., Vuichard, N., Zhou, F., Li, B., Piao, S., Peng, S., Huang, Y., and Tao, S.: Global forest carbon uptake due to nitrogen and phosphorus deposition from 1850 to 2100, Global Change Biology, 23, 4854-4872, doi:10.1111/gcb.13766, 2017.

Whitfield, C. J., and Reid, C.: Predicting surface area of coarse-textured soils: Implications for weathering rates, Canadian Journal of Soil Science, 93, 621-630, 2013.

Wösten, J. H. M., Pachepsky, Y. A., and Rawls, W. J.: Pedotransfer functions: bridging the gap between available basic soil data and missing soil hydraulic characteristics, Journal of Hydrology, 251, 123-150, https://doi.org/10.1016/S0022-1694(01)00464-4, 2001.

Yang, X., Post, W. M., Thornton, P. E., and Jain, A. K.: Global Gridded Soil Phosphorus Distribution Maps at 0.5-degree Resolution. ORNL Distributed Active Archive Center, 2014.